INFORMATION TO USERS

This manuscript has been reproduced from the microfilm master. UMI films the text directly from the original or copy submitted. Thus, some thesis and dissertation copies are in typewriter face, while others may be from any type of computer printer.

The quality of this reproduction is dependent upon the quality of the copy submitted. Broken or indistinct print, colored or poor quality illustrations and photographs, print bleedthrough, substandard margins, and improper alignment can adversely affect reproduction.

In the unlikely event that the author did not send UMI a complete manuscript and there are missing pages, these will be noted. Also, if unauthorized copyright material had to be removed, a note will indicate the deletion.

Oversize materials (e.g., maps, drawings, charts) are reproduced by sectioning the original, beginning at the upper left-hand corner and continuing from left to right in equal sections with small overlaps. Each original is also photographed in one exposure and is included in reduced form at the back of the book.

Photographs included in the original manuscript have been reproduced xerographically in this copy. Higher quality 6" x 9" black and white photographic prints are available for any photographs or illustrations appearing in this copy for an additional charge. Contact UMI directly to order.

UMI

A Bell & Howell Information Company
300 North Zeeb Road, Ann Arbor MI 48106-1346 USA
313/761-4700 800/521-0600

Université d'Ottawa · University of Ottawa

Multilayer Adsorption of Water on Rutile (110)

by

Bruno J. Riel

Thesis
presented to the School of Graduate Studies and Research
of the University of Ottawa
in the fulfillment of the thesis requirements
for the degree of

Master of Science in Physics

University of Ottawa
Ottawa, Ontario
January 31, 1997

ABSTRACT

The adsorption of water on the (110) surface of rutile is investigated by recording Thermal Desorption spectra, and characterizing the substrate using Low Energy Electron Diffraction. The sample is sputtered and annealed according to a previous flattening study of the same surface. After cooling to T ≈ 110K, the surface is dosed with H_2O. The adsorbate/substrate system is heated at 1K/s, and the H_2O partial pressure is measured with a shrouded quadrupole mass spectrometer. Three desorption peaks are observed below room temperature, two monolayer peaks: one at 310-260K (coverage dependence) and another at 175K, and one multilayer peak at 150K. A fourth peak, representing a coverage of the order of a few percent of a monolayer, is observed at T ≈ 500K; this peak is associated with an adsorption state that is more strongly bound than the other three. Analysis of the first three adsorption states provides information on the kinetics of the system, and the bond energies at these adsorption sites.

ACKNOWLEDGMENTS

I would like to express my sincere gratitude to Dr. Peter Piercy, my research supervisor, for his support, guidance and continued encouragement, but mostly for believing that I could do the work. Working with him has been extremely rewarding.

I would also like to thank Karin, my partner in physics, and in life. Without her presence and encouragement, I probably would not have finished this work, and I certainly would not have submitted this thesis on time. Thanks for the equations and the figures.

As well I thank: Dr. Brian Hird: for giving me my first chance to work in a research lab, and for introducing me to surface physics; Jennifer Seel: for also working on TiO_2; Dr. Bruno Grossmann and Luke Doran: for their help in the lab; Grant Nixon and Dr. Serge Desgreniers: for making teaching in the 3rd year labs a nice experience; Louis-Philippe Massé: for helping out with MS-Word; Matt Dowd: for helping out with other software; Jacques M. Laniel for showing me how to use a scanner and double checking some of the derivations; Sylvain Hubert: for help with yet other software; and Mitch Boileau: for his collegiality.

This work is dedicated to my parents, Aurèle and Jeannine,
very simply, for everything.

TABLE OF CONTENTS

LIST OF FIGURES

CHAPTER 1
INTRODUCTION

1.1 General Motivations

In recent decades there has been an increase in the recognition of the importance of surface phenomenon and surface effects in all areas of science. The major surface physics interests are in heterogeneous catalysis, semiconductor devices, and metallurgy. The discussion of these three points that follows in the rest of this introduction pertains mostly to "concrete applications" of surface science. With this said, we should not forget that there has always been a need for fundamental research as a mean of increasing our general knowledge in a given area. Historically research in the solid state centered on the bulk and its properties, but now, we are beginning to have a consistent picture of the physics of the surface and its relation to the bulk.

Metallurgy is concerned with the surface of materials in two major areas: corrosion, and mechanical failure. Both involve surface science in a similar manner. We can consider a free surface to be the meeting of a material (solid phase) with its environment (gas or liquid), whereas a grain boundary is the meeting of two solid materials (or two different phases of the same material). In this regard both a free surface and a grain boundary can be understood as surfaces. Corrosion often appears at a free surface, whereas mechanical failure often occurs at a boundary interface (internal surface). In both cases the electronic states, and the chemical interactions at the surface

are of great interest, and the study of single crystal surfaces, which are usually simpler systems, can provide much information.

Another industry in which interface boundaries come into play is that of semiconductor devices. Most modern electronic components are based on the properties that arise when two semiconductor materials are put into contact. Usually these devices are extremely small and in consequence the surface effects become considerable. Also, one of the most important techniques used in the construction of devices and components is MBE (Molecular Beam Epitaxy). This technique of growing one material onto a substrate by some "evaporation process" involves chemistry and physics at the surface of materials through phenomena like adsorption, reconstructions, order-disorder phase transitions, flattening, . . .

The chemical industry, as any industry, has always been in search of cheaper, faster, and hopefully cleaner, methods of production. The use of solid catalysts, usually in the form of powders, is now fairly common; this has created a need for a greater understanding of reactions at solid surfaces. These reactions involve adsorption (the bonding of molecules at the surface in question), surface interactions, and desorption (the activated process by which the adsorbed molecule leaves the surface). The solids used as catalysts need not always be powders: often reactions involve metallic alloys or sometimes single crystals. Perhaps the most common use of an alloy as a catalyst is the catalytic converter found under all modern automobiles. This device is a platinum based alloy organized in a high surface to volume ratio configuration that further oxidizes molecules like CO and NO (this could further lead us into a discussion of environmental science).

Other types of chemical reactions can also involve solids. In the early '70's Fujishima and Honda electrolyzed water with a system of two electrodes, one of which

was TiO_2, connected with a wire, but without the use of a battery in the circuit. They achieved this simply by shining light onto the TiO_2 electrode. That was the beginning of the great interest in the interaction of H_2O with oxide surfaces (and large band gap semiconductors). In direct relation to the work carried out to prepare this thesis, it was the origin of the drive to understand the adsorption of H_2O on TiO_2.

1.2 A Few Concepts

What do we mean when we speak of a surface? Clearly we do not mean the two dimensional mathematical object. It is perhaps best to proceed from the concept of selvedge; the Random House Dictionary gives for this word the following definition: "the edge of woven fabric finished so as to prevent raveling." With this in mind we can call the selvedge of a material its last few atomic layers in which the electronic and possibly structural properties differ due to the termination. This analogy is correct in the sense that the properties of the material adjust themselves away from bulk behavior to minimize surface free energy, and in particular to keep the free electrons in the material. We can then picture the surface as being the upper layer of the selvedge.

When a sample is put into contact with a gas, the total exposure is proportional to the number of molecular impacts per unit area of the sample surface. Exposure is often expressed in units of Langmuir (L). One Langmuir is defined as 10^{-6} Torr·s, and represents 3.8×10^{14} impacts per square centimeter.

Adsorption is the bonding of molecules onto a surface. By bonding we mean that the adsorbed molecule is "trapped" in some manner and remains on the surface. In the case of a one Langmuir exposure, assuming a sticking, or trapping, probability of 100%, the coverage of the sample surface by the adsorbed layer would be of the order of 1 adsorbed particle per unit cell of the surface mesh. Assuming a square unit cell about 10^{-15} cm^2 in area (3 $Å^2$), this gives us 10^{15} sites per unit square centimeter (here we can see the convenience of the Langmuir).

The adsorption bond may be rather weak (<< 25 meV, kT room temperature), in which case we speak of physisorption, or it may be strong, in fact comparable to molecular bonds (order of 1 eV), and we then speak of chemisorption. This is not to say that the intermediate energies are excluded; we shall in fact see later on that H_2O on TiO_2 falls in this range. The most general way of describing all adsorption is to simply speak of the adsorbate being trapped in a potential well at the surface, and to leave for specific models the exact nature of the actual bond.

The presence of an adsorbate on the surface of some materials can cause a reconstruction of the selvedge, or it may undo an existing one. The expression: surface system, can be used when it is convenient or necessary to speak of the adsorbate and the selvedge as one unit.

In the previous section we described desorption as the activated process by which an adsorbed molecule leaves the surface. In keeping with our simple picture of trapping in the surface potential well, we need only say that some mechanism transfers energy to the adsorbate, and that when this adsorbed particle is sufficiently excited it leaves the adsorbate and returns to the gas phase in contact with the sample.

Plots of the partial pressure of the desorbing gas versus the sample temperature are commonly called thermal desorption spectra. This is not a complete misnomer as the

position of the desorption peaks does relate to the trapping energy of the adsorption state. The total area under such a curve, in units of pressurextime, will be proportional to the total initial coverage, or amount dosed and trapped, on the sample.

Any other uncommon terms will be defined as they are encountered in the text, but, before we move on to the next section, we will introduce one last concept: the monolayer. A monolayer can be, and has been, defined in many different manners. The most simpleminded approach is to assume a "hard sphere" type cross sectional area for the free molecular state of the adsorbate, and divide the total surface area of the sample by this value; this is usually of limited physical meaning. A second approach is to define a priori a monolayer as consisting of an integer number of adsorbed particles per unit cell of the surface mesh; the precise value of the integer is then related to the specifics of the model and the precise calibration of the quantities desorbed. In this way peaks can be seen to saturate at fractional coverages. If an absolute coverage calibration is not available, and one is mostly interested in the energetics of the system, there is a third approach: conversely to the second approach we have just described, it is possible to arbitrarily take the first desorption peak in the desorption spectra that saturates with increasing exposure, or dose, as being coverage equal to one monolayer. This last definition can later be related to a specific model and the surface structure, essentially this then brings us back to the second approach. We followed the third of these definitions.

1.3 Material: TiO_2

TiO_2 can be found in three different crystal structures: anatase, brookite, and rutile. It is a very abundant material, indeed it is used as an abrasive agent in some brands of toothpaste, and in its anatase form as a white pigment in many commercially available paints. For our experiments we used a single crystal rutile sample cut along the plane of the (110) surface[1.1].

The (110) surface of TiO_2 is expected to have bulk like termination; this is supported by MEED (Medium Energy Electron Diffraction) evidence[1.2]. We therefore begin by describing the bulk structure.

Looking at figure 1.1, we can see the tetragonal structure of the rutile lattice. To first approximation, the Ti cations are quadruply ionized, and the O anions are doubly ionized. The O^{2-} are in a quasi-perfect octahedral structure, and half of these octahedra are occupied by Ti^{4+} in their center.

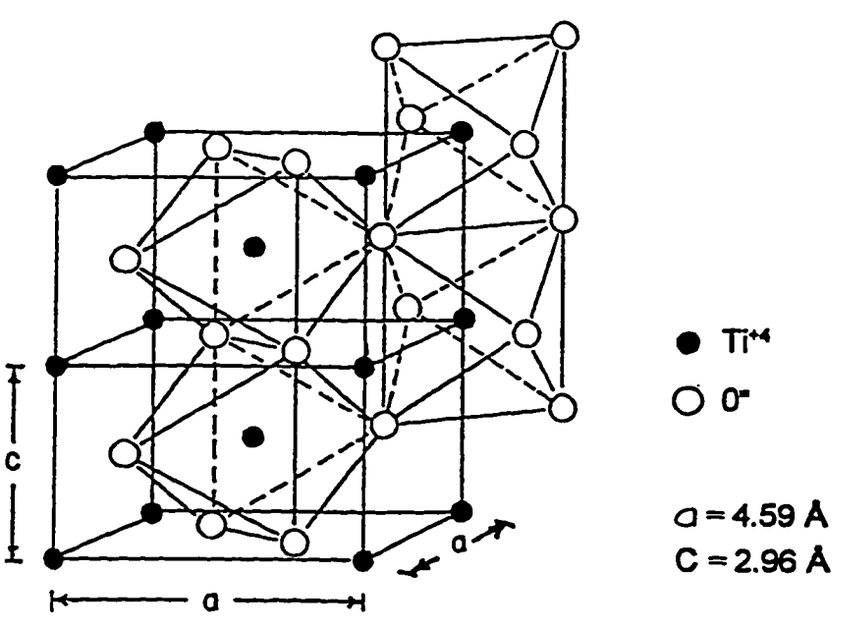

Fig. 1.1 The bulk unit cell [1.5].

The conduction band is derived from the 3d levels of the Ti cations, and the valence band is derived from the O anion 2p levels. The bulk bandgap region is 3.1 eV wide. Excluding the electronic states associated with defects created by the fracturing process, the band gap is free of surface electronic states. Annealing in UHV reduces the sample; this pins the Fermi level at the bottom of the 3d conduction band and increases the conductivity in the bulk.

Of all the low index planes, it is the (110) that offers the most stable surface. The accepted (110) surface structure and termination can be seen in figure 1.2.

On a small scale this surface can be considered to be non-flat, because of its rows of oxygens that constitute a set of parallel ridges along the surface.

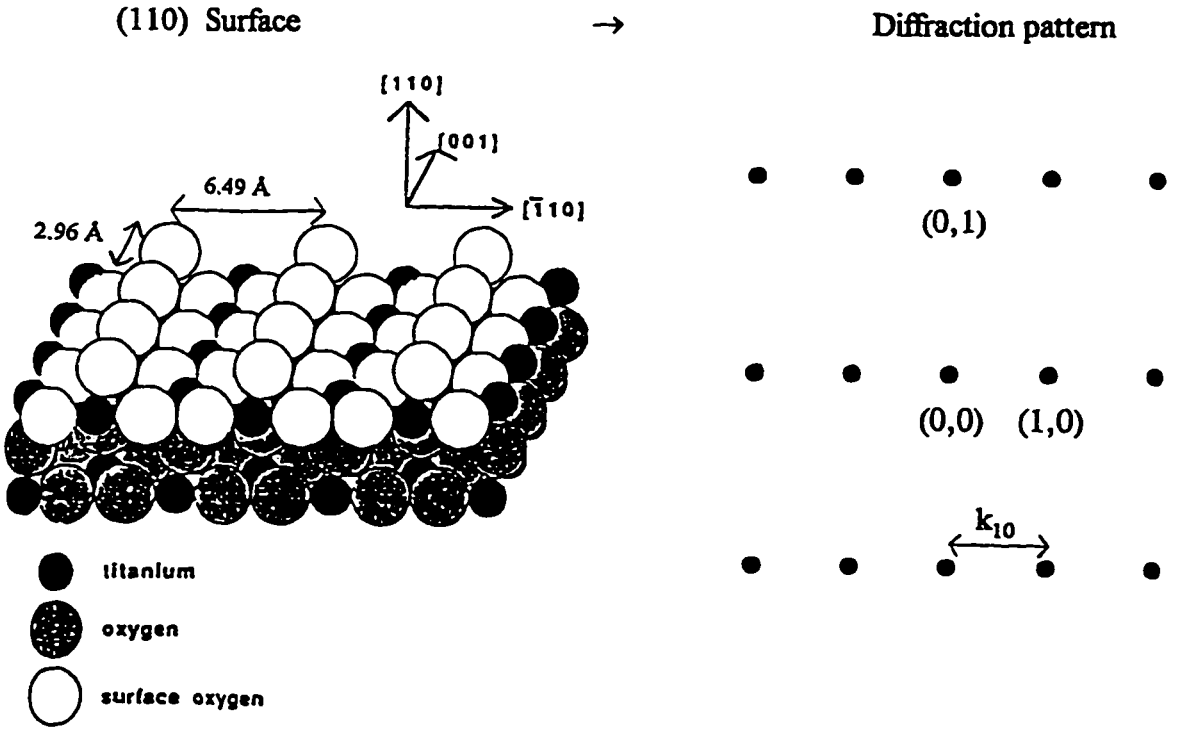

Fig. 1.2 The possible surface structure described in the text. The [001] direction is also referred to as a_1 (its associated reciprocal space direction as a_1*), and similarly [$\bar{1}$10] is referred to as a_2 (reciprocal a_2*) [1.2].

This is the preferred model for the surface because it would be formed by breaking the smallest number of cation-anion bonds. It is populated by an equal number of Ti^{4+} having five O^{2-} ligands and others having the full six coordination. The resulting surface, having equidistant rows (or planes) of ions above and below the plane of the surface, is non-polar.

Most surface preparation recipes produce a (1×1) surface structure. The fact that vacuum fracture, conventional polishing, sputtering and annealing (in O_2 or vacuum) all produce the (1×1) surface is due to the great stability of this surface. In fact other planes, including the (001) surface are seen to facet into (110). Furthermore, contrary to many other materials TiO_2 does not require vacuum fracture to produce a stoichiometric surface. A (2×1) and other more complex reconstructions have been produced (by Piercy et al. and by other teams) using a number of different recipes, most of which involve long anneals (> 1 hour) at high temperatures (> 1100K).

The unreconstructed (110) surface has been the most extensively studied of TiO_2 surfaces.

1.4 Past Efforts, Other Research Teams

Although the adsorption/desorption of a variety of gasses has been studied on the surfaces of TiO_2, we present only the work done by two teams of researchers as context for this thesis, the studies of: H_2O on TiO_2 (100) by Henderson et al.[1.3], and H_2O on TiO_2 (110) by Campbell et al[1.4].

Campbell et al. observed four (possibly five) desorption peaks. The first peak appeared at 300K in their TDS spectra for the lowest coverages and moved to 260K with increasing coverage. They attributed this to molecularly adsorbed H_2O at Ti^{4+} sites (based on XPS and work function measurements). They determined an activation energy for desorption from this state by utilizing the Arrhenius activated kinetics equation, assuming first order kinetics and assuming a pre-exponential factor equal to $10^{12}\ s^{-1}$; they found a coverage dependent value of $71-9\cdot\theta$ kJ/mol, (θ is the symbol commonly used for coverage). Using the O(1s) signal in their XPS measurements they evaluated the saturation coverage of this site to be about one H_2O molecule per Ti^{4+} exposed surface cation, or one per surface unit cell. Their reconstructed peak shape did not manage to explain the high temperature tail measured for this peak. Again, using the XPS measurements they surmised that this tail might be due to the disproportionation of surface hydroxyl groups. Increasing water doses further, they found a second peak at 170K, and then one at 160K. Finally they found one last peak at 500K, which they attributed to the disproportionation of hydroxyl groups bound to thermally induced oxygen vacancies of about 1% surface concentration.

Henderson et al. studied the adsorption of H_2O on both the (1×1) and (1×3) structures of the (100) TiO_2 surface. The (1×1), or unreconstructed, surface shows bulk termination and contains only one type of Ti cation site. The (1×3) reconstruction of the same surface has (110) microfacets and contains three types of Ti cation sites. They

calibrated their water doses by using a "conduction limited measurement" (of which we will not go into details) and determined that because essentially all the H_2O came into contact with the sample surface, the exposed dose was equal to the total amount of H_2O exiting their doser. For both of these surfaces and for all water coverages the only desorption species detected between 130-800K was molecular water. They noted that if any water had been adsorbed in a dissociated form, it must have recombined into H_2O during desorption; they affirmed this because they believed that the water detected desorbing from the surface could account for all the water to which the surface had been exposed during the dosing process.

The spectra obtained from the (1×1) surface showed four peaks below room temperature: one with coverage dependent position from 340-320K (θ=1 H_2O molecule per ~ 3.3 Ti^{4+}, $2{,}2\times10^{14}$ molecules/cm^2 or 0.3 ML (monolayer) by their calibration), a second with coverage dependent position again from 280-250K, prior to saturation of peak 2 a third peak starts to grow in at about 180K, and finally a fourth peak at 165K. The total coverage of the three first peaks at saturation was approximately 7.5×10^{14} molecules/cm^2, which is close to the surface number density of five-coordinate Ti^{4+} cations; this added to the weak non-coverage dependent binding of the 165K peak suggested to them that the first three peaks are associated with water binding in the first layer whereas the fourth peak binds as a second layer. Through assumptions about surface chemistry on TiO_2, and some spectroscopic evidence produced by other teams, they attribute the 350K peak to dissociative adsorption, and the 250K peak to molecularly adsorbed water.

For doses of ~ 0.30 ML or less the (1×3) showed desorption spectra similar to those of the (1×1): a single peak at about 330K. Using the "Threshold Method", which we shall discuss in the analysis section, they determined a desorption energy of 18 kcal/mol. Beyond doses of 0.3 ML the spectra for the (1×3) differed from that of the

(1×1). Where, as coverage is increased, a second peak begins to grow at 250K in the spectra for the (1×1) surface, the (1×3) feature at 330K gradually shifts to 238K (going from near zero coverage to monolayer coverage: 333-238K), but no second feature appears until larger than single monolayer coverage is reached. Near saturation of the monolayer peak (similarly to the (1×1) surface) a second peak appears just below 200K and continues to grow after saturation of the first monolayer. The desorption at low temperature from the first monolayer was not resolved from the desorption of the second layer so that this feature did not saturate as in the case of the (1×1) surface.

Henderson also attempted to fit the single peak (at ~ 330K) for coverages < 0,3 ML in both sets of TDS spectra to second order desorption kinetics using "reasonable" pre-exponential factors and energies in the Arrhenius formula. Constant parameters could not reproduce the observed coverage dependence across all the spectra for either surface, and they concluded that coverage dependence was required in the set of parameters.

All the experiments done with calibrated coverages indicate that H_2O adsorbs with a sticking probability of ~100%, or in other terms, a sticking coefficient of 1. Another general comment that can be made about the studies is that no past dosing history dependence was noticed in any of the spectra.

Our work is an attempt at acquiring, on the TiO_2 (110) surface, higher quality water desorption data and producing more rigorous an analysis. This should serve to improve the reliability of the numerical results obtained and possibly lead to a better agreement between TDS spectra reconstructions and their experimental equivalents. In the final sections of this thesis we shall return to some of the work of these research groups and discuss their findings in greater detail, and compare our results to theirs.

CHAPTER 2
THEORY

2.1 Adsorption/Desorption Phenomenon

2.1.1 Surface Potential Well

Chemisorption on metal oxide surfaces is dominated by the ionic nature of the exposed surface atoms; because of this, the chemisorption reaction can be likened to acid-base or oxidation-reduction chemical reactions. In the case of acid-base reactions, the surface cations can act as an acid, or electron acceptor, whereas the anions can act as a base, or electron donor, and of course the adsorbate will bond at sites having the character opposite to its own. Acid-base adsorption reactions do not require electron exchange, but involve the overlap of a filled orbital on the donor with an empty orbital on the acceptor; bonding and anti-bonding levels are formed and the electrons go to reside in the bonding levels first, and this reduces the total energy of the system. On the contrary, the oxidation-reduction adsorption reaction involves charge exchange.

In the case of the weaker bonding involved in physisorption, the surface-adsorbate attraction can be attributed to the dipole interaction (Van der Waals effect) as well as higher order terms of the electric multipole interaction.

We can present three broad classifications for the adsorbate-surface bonding interaction; they are: (1) polar (ion-dipole or fluctuating dipole), (2) donor-acceptor, (3) oxidation-reduction. An actual adsorption reaction will not necessarily have the true or complete nature of any of these classes, rather, we should interpret these three divisions as three points in a continuous spectrum of surface-adsorbate bonding interaction. Such a spectrum of interaction can be described in quantum mechanical terms as ranging from slight to great wavefunction overlap, with the proper energetics determined by the occupation of the involved energy levels: no overlap, overlap, hybridization.

There is another important characteristic of the adsorption phenomena that we should mention: dissociation. In certain cases it is energetically favorable for an adsorbing molecule to dissociate during the adsorption reaction. In these cases, the bonding interaction is usually quite strong.

The repulsive force experienced by an adsorbing particle as it approaches the surface to within a few angstroms must be dealt with by microscopic modeling such as: density functional theory for atoms adsorbing on metals, and two-body forces summed over the system for atoms adsorbing on molecular or ionic solids. Of course, detailed quantum mechanical modeling of many body systems can attack both repulsive and attractive considerations at once. The main point of this section is this: Through some interaction there exists a potential well with a minimum at a close distance to the surface that "traps" the adsorbate onto the surface. Some examples of adsorption potential wells can be found in figure 2.1.

In the water molecule, the two filled orbitals of the oxygen atom not linked with the two hydrogens represent two lone pairs of electrons that allow the oxygen to act as an electron donor –of course as described a few paragraphs back the magnitude of the electronic interaction can vary greatly. Two other characteristics of the water molecule

that come into play in its interactions are the fact that it is a polar molecule and therefore has a permanent dipole, and its ability to hydrogen bond with other water molecules.

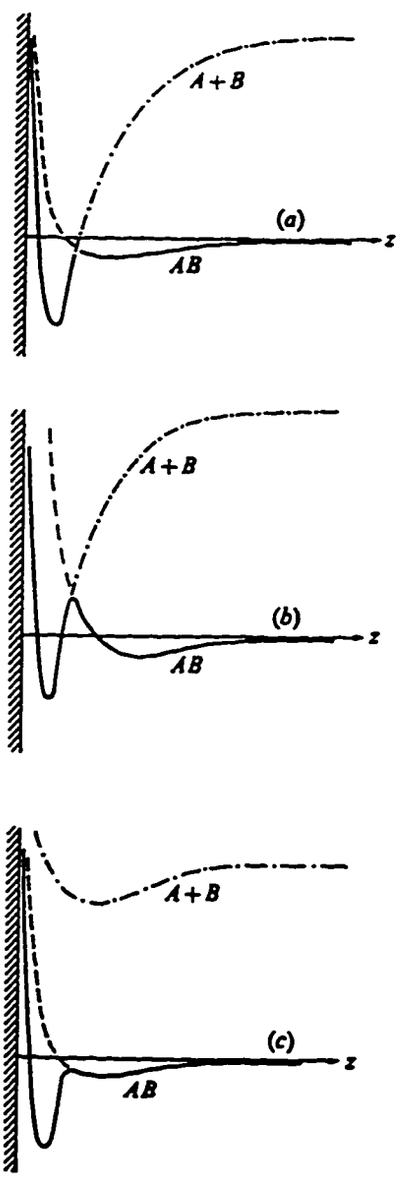

Fig. 2.1 Schematic diagrams of the potential energy of an absorbate/substrate complex appropriate to three different ground state configurations: (a) dissociative chemisorption; (b) molecular physisorption; (c) molecular chemisorption (Lennard-Jones, 1932) [2.1].

The TiO_2 (110) surface unit cell presents one Ti^{4+} that does not have the full six O^{2-} coordination; this cation is therefore apt to act as an electron acceptor in an acid-base type reaction. The fully coordinated Ti^{4+} ions are hidden behind the topmost surface oxygens. The dominant type of surface defects are oxygen vacancies; the site associated with each of these absent oxygens must be negatively charged to maintain charge neutrality and therefore could present a strong bonding site. These defect sites are often referred to as Ti^{3+} sites, but the additional negative charge is in fact expected to be shared with all the neighboring Ti cations

2.1.2 Desorption as a Phonon Mediated Process

Here we present a model of desorption. What follows is a description of the theoretical work done by Kreuzer et al; they studied desorption as a Markovian process. We choose this model because it leads to corroboration of the use of the Arrhenius form for the rate of desorption. We begin by heuristically justifying the choice of this stochastic mechanism; for a more detailed description of this model see[2.2].

A particle trapped in the potential well we presented in the last section will oscillate in the direction perpendicular to the surface with an energy of order kT. The particle is in a well-defined energy state most of the time, but when the particle moves closer to the surface there is an increased probability that the quantum mechanical state of the particle will be changed by a phonon mediated energy exchange mechanism. This can be attributed to the fact that contributions to the transition probability per unit time, Fermi's Golden Rule, are greater closer to the surface because the $\langle \psi_{n+1} | \delta V | \psi_n \rangle$ matrix element is greater due to the steepness of the potential. In other words, at such close

proximity to the surface the potential quickly becomes repulsive, and therefore the time spent close to the surface is much shorter than the time spent in each well defined energy state. This is why we can consider the coupling to phonons to be a perturbation on the system, and hence call on Fermi's Golden Rule to describe the transition probabilities in the well.

This type of random hopping from state to state is a characteristic of stochastic processes. Furthermore, the surface has a thermal relaxation time that is also much shorter than the duration of each well defined energy state. Combined with the bulk the surface acts as an infinite thermal bath so that the thermal distribution of phonons is not affected by the presence of the adsorbed particle. The only aspect of the system that varies is the energy state of the particle and therefore the phonon mediated energy transfer mechanism is strictly dependent on the state that the particle is in at the time of the energy exchange. This lack of history dependence in the system suggests that we are dealing with a Markov process.

The Markov master equation for the adsorbate can be written as:

$$\frac{\mathrm{d}n_i}{\mathrm{d}t} = \sum_{i'}\left[W(i,i')n_{i'}(t) - W(i',i)n_i(t)\right] + \sum_k W(i,k)n_k(t) - \sum_k W(k,i)n_i(t) \qquad (2.1)$$

where the i's denote states in the adsorption well, the k's denote states in the gas phase in contact with the surface, the n's are occupation probability densities, and $W(b,a)$ is the transition probability from state a to state b.

At this point two assumptions must be made: (1) the temperature variation during our experiment is slow enough that the substrate (but not the adsorbate) can be considered in thermal equilibrium at all times (this only requires that the time scale of the temperature ramp of the sample involved be much slower than the surface thermal

relaxation time and the time scale of the energy exchange mechanism), and (2) that the gas is pumped away fast enough that all $n_k(t)=0$. The initial conditions are:

$$n_i(t<0)=n_i^{eq} \tag{2.2}$$

$$n_k(t>0)=0 \tag{2.3}$$

The second assumption destroys detailed balance in the system, that is, we can no longer write:

$$W_{ik}\,n_k^{eq}=W_{ki}\,n_i^{eq} \tag{2.4}$$

although, the matrix $W(i, i')$ still satisfies detailed balance in the subspace (i,i').

We implement equation (2.3), and write:

$$\frac{\mathrm{d}n_i}{\mathrm{d}t}=\sum_{i'}\left[W(i,i')n_{i'}(t)-W(i',i)n_i(t)\right]-\sum_k W(k,i)n_i(t) \tag{2.5}$$

$$\frac{\mathrm{d}n_i}{\mathrm{d}t}=\sum_{i'}W^{total}(i,i')n_{i'}(t) \tag{2.6}$$

The lowest eigenvalue, λ_0, of $W^{total}(i,i')$ is nonzero but much smaller than all the other eigenvalues if $W(k,i)<<W(i,i)$. To relax this condition, one may consider that the lower occupation of the upper levels of the well will make the transition rates sufficiently smaller.

We now use the usual exponential form for the solution of Markov processes, but we explicitly write the difference in scales of the eigenvalues:

$$n_i(t)=f_0 e_i^{(0)}e^{-\lambda_0 t}+\sum_{k>0} f_k e_i^{(k)}e^{-\lambda_k t} \tag{2.7}$$

The λ_k's can be understood as representing transients, and λ_0 as being related to the desorption rate.

We define coverage, θ as:

$$\theta(t) = \frac{N_g}{N_s A} \sum_i n_i(t) \tag{2.8}$$

where A is the surface area, N_s is the maximum surface density of particles adsorbed in a monolayer, and N_g is the total number of gas particles. By differentiating with respect to time, we get the rate of change in coverage:

$$\frac{d\theta(t)}{dt} = \frac{N_g}{N_s A} \sum_i \frac{dn_i(t)}{dt} \tag{2.9}$$

$$\frac{d\theta(t)}{dt} = \frac{N_g}{N_s A} \sum_i \left\{ \sum_{i'} \left[W(i,i') n_{i'}(t) - W(i',i) n_i(t) \right] - \sum_k W(k,i) n_i \right\} \tag{2.10}$$

The first term in the summation represents the transitions from bound state to bound state, and therefore does not contribute to changing θ; it is canceled by summing over i. Therefore:

$$\frac{d\theta(t)}{dt} = -\frac{N_g}{N_s A} \sum_{i,k} W(k,i) n_i(t) \tag{2.11}$$

Now, if the transition rates into the gas phase are much slower than the transition rates within the well, then the total occupation of the potential well energy levels will vary slowly enough for the occupation density distribution to always be equilibrium-like. The transitions into the gas phase "move the equilibrium along", that is, although the total occupation is changing with time, the distribution retains its equilibrium shape. To express this, we write an ansatz for the time variation of the occupation probability:

$$n_i(t) = \frac{\sum_i n_i(t)}{\sum_{i'} n_{i'}^{eq}} n_i^{eq} \tag{2.12}$$

in which we can replace the sum in the numerator by using equation (2.8), and get:

$$n_i(t) = \theta(t) \frac{N_s A}{N_g} \frac{n_i^{eq}}{\sum_{i'} n_{i'}^{eq}} \tag{2.13}$$

and therefore, the rate of change in coverage, equation (2.11), becomes:

$$\frac{d\theta(t)}{dt} = -\frac{\sum_{i,k} W(k,i) n_i^{eq}}{\sum_{i'} n_{i'}^{eq}} \theta(t) \tag{2.14}$$

this is the quasi-equilibrium approximation for the desorption rate.

We continue by assuming that the particles follow Maxwell-Boltzmann statistics:

$$n_j^{eq} = \frac{1}{N_g} \frac{1}{e^{\beta (E_j - \mu) \pm 1}} \qquad \begin{pmatrix} + & \text{Fermi-Dirac} \\ - & \text{Bose-Einstein} \end{pmatrix} \tag{2.15}$$

in which j stands for either i or k, and $\beta = kT$. In the usual limit:

$$n_i^{eq} = \frac{1}{N_g} e^{-\beta (E_j - \mu)} \tag{2.16}$$

Using this and detailed balance, we get:

$$\dot{\theta}(t) = -\frac{\sum_{i,k} W(i,k) e^{-\beta E_k}}{\sum_i e^{-\beta E_i}} \theta(t) \tag{2.17}$$

Finally, we approximate the denominator by the highest contribution in the sum to get:

$$\dot{\theta}(t) = -\sum_{i,k} W(i,k) e^{-\beta E_k} \cdot \theta(t) \cdot e^{-\beta V_0} \tag{2.18}$$

where V_o is the depth of the adsorption potential well.

If we now define a prefactor:

$$\nu = \sum_{i,k} W(i,k)\, e^{-\beta E_k} \tag{2.19}$$

we can write the expression for the rate of change in coverage as the recognizable Arrhenius form:

$$\dot{\theta} = -\nu\, \theta\, e^{-\beta V_0} \tag{2.20}$$

2.1.3 Kinetics of Desorption

In the basic interpretation of the kinetics of reaction rates, the prefactor in the Arrhenius form for the desorption rate is taken to be an attempt frequency, literally a vibration along the surface normal. Clearly from the result of the last section the pre-factor has a more subtle meaning, including in fact the transition probabilities into the gas phase from the energy levels in the adsorption potential well, which may be dependent on surface coverage. It also depends on the energies to which the particles desorb in the gas phase, but the range of these energies is only very weakly dependent on temperature, being of order kT (and the temperature ramp, dT/dt, is so slow as to be isothermal-like), and are not dependent on surface coverage.

In our analysis we will use a generalized Arrhenius form:

$$\frac{d\theta}{dt} = -\nu_{eff} \cdot e^{-E/kT} \tag{2.21}$$

where ν_{eff} is an effective prefactor that we will attempt to relate to kinetics of order n with: $\nu_{eff} = \nu\theta^{n}$. Detailed analysis may demonstrate the possible dependence of both ν and E on the surface coverage.

2.1.4 Thermodynamic Perspective

In this section we shall derive an expression for the isosteric heat of adsorption determined from desorption kinetics data using thermodynamic considerations. We begin with the Clausius-Clapeyron equation for an adsorbate at constant adsorbed number and surface area:

$$\left(\frac{\partial P}{\partial T}\right)_{Na,\,A} = \frac{\overline{S}_g - \overline{S}_a}{\overline{V}_g - \overline{V}_a} \tag{2.22}$$

next we write the enthalpy change due to taking one molecule from the adsorbed phase to the gas phase:

$$\mathrm{d}H = T\,\mathrm{d}S - V\,\mathrm{d}P \tag{2.23}$$

$$\overline{H}_a - \overline{H}_g = T\left(\overline{S}_a - \overline{S}_g\right) \tag{2.24}$$

and therefore, we can rewrite this using the Clausius-Clapeyron equation:

$$\overline{H}_a - \overline{H}_g = T\left(\overline{V}_a - \overline{V}_g\right)\left(\frac{\partial P}{\partial T}\right)_{Na,\,A} \tag{2.25}$$

Now, since $\overline{V}_a$ is much smaller than $\overline{V}_g$, and taking the ideal gas expression for $\overline{V}_g$, we can write the isosteric heat of adsorption (enthalpy/particle) as:

$$Q = \frac{kT^2}{P}\left(\frac{\partial P}{\partial T}\right)_{Na,\,A} \tag{2.26}$$

or

$$Q = kT^2\left(\frac{\partial \ln P}{\partial T}\right)_{\theta} \tag{2.27}$$

where P is the equilibrium vapor pressure of the adsorbate with coverage θ at temperature T.

The adsorbate and the gas phase are in equilibrium, that is:

adsorption rate per unit area = desorption rate per unit area (2.28)

The adsorption rate is proportional to pressure and a sticking coefficient. The total desorption rate per unit area is equal to the desorption rate normalized per site (r_d) multiplied by the number of sites on the sample (N_0) and divided by the sample area (A); it is a property of the adsorbate of $N_0 \times \theta$ particles. Therefore, we have:

$$S(\theta,T)\frac{P}{(2\pi\, mk\, T)^{1/2}} = \frac{r_d(\theta,T)\, N_0}{A} \tag{2.29}$$

$$P = \frac{constant \cdot r_d(\theta,T) \cdot T^{1/2}}{S(\theta,T)} \tag{2.30}$$

and therefore we can write:

$$Q = k\,T^2\left(\frac{\partial \ln\left(r_d(\theta,T)\right)}{\partial T}\right)_\theta + \frac{k\,T}{2} - k\,T^2\left(\frac{\partial \ln\left(S(\theta,T)\right)}{\partial T}\right)_\theta \tag{2.31}$$

Again, as in the final result of the previous section, we see that in principal the thermal energy comes into play. If we look at the expression we have just derived, and consider that in most adsorption systems and certainly in the case of chemisorption, the $kT/2$ (~ 0.025 eV/2) term is negligible compared to the energies involved (order of 1 eV). The third term, the dependence of the sticking coefficient on temperature, will vary greatly from system to system. In the case of the water molecule, its sticking coefficient on most surfaces is close to one, and no evidence exists for it being dependent on temperature in the case of water on TiO_2. (A study of the sticking coefficient would require calibrated coverage measurements, and calibrated dosing. More will be said on coverage and dosing in the following chapters.) In our case, we therefore can write the desorption energy as:

$$E_d = k\,T^2\left(\frac{\partial \ln\left(r_d(\theta,T)\right)}{\partial T}\right)_\theta \tag{2.32}$$

This final result is a macroscopic thermodynamic quantity, and it was derived without assuming any microscopic model or picture. The interpretation of the "desorption energy" in terms of a one particle dynamical model at a single site is therefore not necessary. The parameters obtained in the analysis (in the final sections of this thesis) will serve first and foremost to described the "goings on" at a certain temperature for a certain coverage on our sample surface as a whole.

2.2 Surface Characterization

2.2.1 Electrons and Surfaces

Electron based probing techniques are the mainstay of surface science research. This is because of their surface sensitivity. Electrons having a kinetic energy between about 5 and 2000 eV that are detected coming from a material, regardless of the mechanism by which they were generated, must originate from the surface region. The high probability of inelastic scattering of low energy electrons inside a solid ensures that electrons coming from deeper regions of the material cannot escape.

There are two main types of energy loss mechanisms in operation: single particle electronic excitations, and plasmon scattering. The first of these two can further be divided into two categories: excitations of valence electrons, and excitation of core

electrons. The contribution to the mean free path by the interaction with core electrons (mainly due to the repulsion from the outer shells) is generally about two orders of magnitude smaller than that for either plasmon scattering or valence electron excitation.

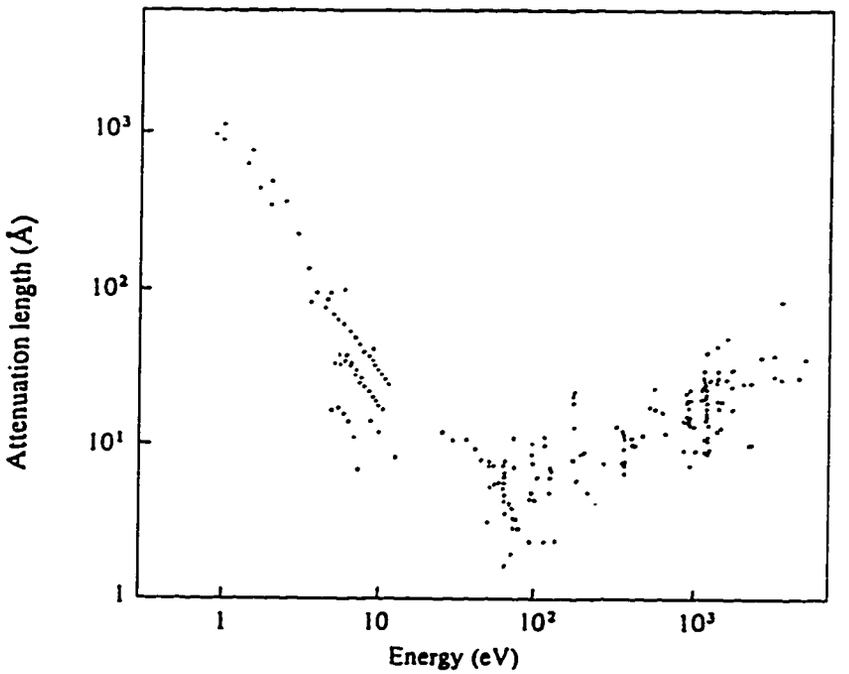

Fig. 2.2 Collection of experimental determinations of attenuation length as a function of energy above the Fermi level for many different materials (after Seah & Dench, 1979). [2.3]

It is therefore the combination of plasmon scattering and valence electron excitation that is the cause for the surface specificity of electron probes, but elastic scattering also contributes. It increases the mean travel distance in the material by reflecting outgoing electrons away from the surface, and although this in itself does not reduce the probability of escape, it increases the probability of the other interactions having their "full effect". We therefore speak of attenuation depth instead of inelastic

scattering mean free path. We will not go into greater details about this since it is not central to our thesis, but we do include a graph of the attenuation depth versus energy (see figure 2.2, the scatter in points is material dependent).

Although it is not a quantitatively important energy loss mechanisms, the interaction with core electrons is not a dead issue. On the contrary it is the basis for one of the two surface characterization techniques that we used in our experiments: Auger Electron Spectroscopy; the other being Low Energy Electron Diffraction. We will now discuss both of these techniques in greater detail.

2.2.2 Auger Electron Spectroscopy

Auger Electron Spectroscopy is a core level spectroscopy used for surface chemical composition analysis. It is based on the ionization of core levels by electrons or X-rays of energy, $KE \geq 1500$ eV. Atoms ionized at these levels will lose energy by filling the empty energy level with an electron from a higher level, and this will be accompanied by the emission of a photon, or an electron. The electron emitted in the second possibility will originate from a level near in energy to the electron that moved down in levels to fill the hole. Electrons emitted in this process are called "Auger electrons". The core hole decay is represented schematically in figure 2.3.

For core hole depths of less then about 10 keV, that is, relatively shallow core levels, the "Auger process" will dominate over the photonic process, and we therefore have an electron spectroscopy as opposed to a light spectroscopy. The core level, as well as the shallower levels are characteristic of the atom involved, and it is therefore possible to identify the atom. (The shallower levels can be core or valence; the core levels, being

less affected by chemical shift are often more useful in this spectroscopy, but valence levels can still be used in the fingerprinting of atoms.)

Auger electrons form a discrete spectrum on top of the smoothly varying background of backscattered/secondary electrons.

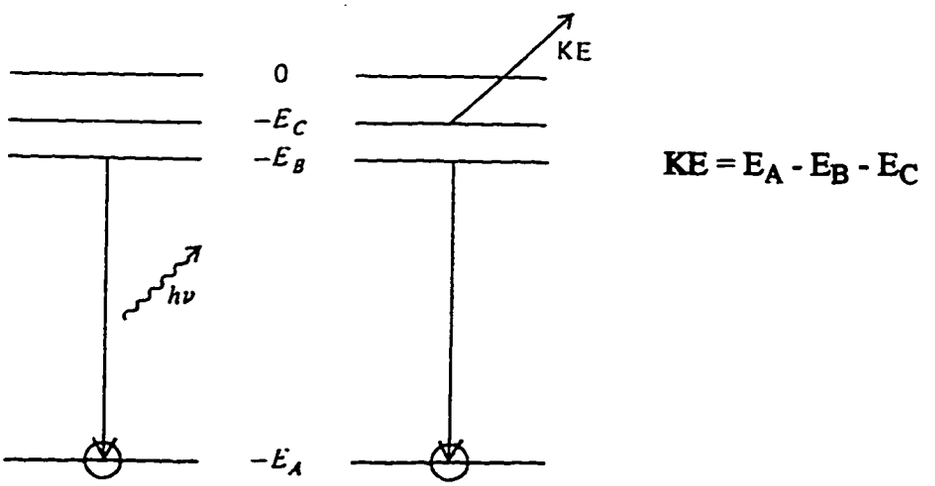

Fig. 2.3 Energy level diagram showing the filling of a core hole in level A, giving rise to (X-ray) photon emission on the left, or Auger electron emission on the right. The levels are labeled with their one-electron binding energies [2.3].

2.2.3 LEED and HRLEED

Low Energy Electron Diffraction is a diffraction technique involving elastically scattered electrons. It is the surface technique equivalent to bulk X-ray diffraction.

Looking back at figure (2.2) we can see that electrons having energies between 10 and a few$\times 10^2$ eV have an elastic mean free path smaller than about 10 Å. On the scale

of crystalline lattice parameters, this is a very small distance; it represents about 2 to 4 atomic layers. Fortuitously these energies also coincide with the energy required for electrons to have an associated de Broglie wavelength of the order of lattice parameters.

The LEED pattern produced is related to the reciprocal surface net which can be calculated from

$$\vec{a}_1^{\,*} = 2\pi\, \vec{a}_2 \times \frac{\vec{n}}{A} \tag{2.33}$$

$$\vec{a}_2^{\,*} = 2\pi\, \vec{n} \times \frac{\vec{a}_1}{A} \tag{2.34}$$

$$A = \vec{a}_1 \cdot \vec{a}_2 \times \vec{n} \tag{2.35}$$

$(\vec{a}_1, \vec{a}_2) \rightarrow$ real space unit vectors

$(\vec{a}_1^{\,*}, \vec{a}_2^{\,*}) \rightarrow$ reciprocal lattice unit vectors

(where $\vec{n}$ is the unit normal to the surface); the LEED pattern will have symmetry that is lower than or equal to that of the real space net. For normal incidence of the electron beam, the point group of the diffraction pattern will be the one of the surface structure (the diffraction pattern is therefore literally the Fourier transform of the real space surface net). Off normal incidence of the electron beam will reduce the symmetry of the diffraction pattern (at least by loss of reflection symmetry across the plane perpendicular to the plane of the beam and the surface normal).

Because the energies used in LEED render the electrons essentially "blind" to depths greater than a few atomic layers, we can say that effectively the system probed has only two dimensional periodicity. Therefore, in the general conservation of energy for in-coming (unprimed) to out-going (primed) wavevectors: $k^2 = k'^2$, we can separate the components parallel and perpendicular to the surface: $k_{//}^2 + k_{\perp}^2 = k'^2_{//} + k'^2_{\perp}$. We can

also consider conservation of momentum independently in each of these directions: $\bar{k}'_{//} = \bar{k}_{//} + \bar{g}_{hk}$ (where $\bar{g}_{hk} = h\bar{a}_1^* + k\bar{a}_2^*$, and $\bar{a}_1^*$ and $\bar{a}_2^*$ are the reciprocal surface net unit vectors), but $\bar{k}_\perp$ need not be conserved.

This probe can tell us if the long range ordered structure is restored after a sputter and anneal cycle (we shall discuss sputtering and annealing as a method of surface cleaning in Chapter 3). A limitation inherent to this technique is that it is impossible to make the electron wavefront plane over an infinite distance; therefore there exists a finite "transfer width" that limits: 1. the resolution in HRLEED (which we shall discuss presently), and 2. the "information" available in terms of the long range order (since the electron beam cannot probe the entire sample at once).

To study a LEED spot in High Resolution, all that is required is an instrument sufficiently precise in its electronic lens system that the diffraction intensity can be studied over a sufficiently small region of $\bar{k}$ space. Typical lattice parameters are of the order of a few angstroms, and therefore one would expect a High Resolution LEED device to be able to resolve reciprocal distances at least one or two orders of magnitude smaller, that is on the order of 10^{-3} $Å^{-1}$. Since we are talking of reciprocal space, these small inverse-distances will be related to information about long range distances on studied surfaces. For instance, an incident electron energy having an associated wavelength equal to four times the step height on the surface of a probed sample will cause destructive interference in certain spots of the LEED pattern; in such a case, it is possible to obtain information regarding the size distribution of islands differing in height by one lattice parameter step, and therefore not only on long range order along the surface as in LEED, but also on flatness (order perpendicular to the surface).

CHAPTER 3
EXPERIMENTAL SETUP AND METHOD

3.1 Vacuum Chamber

The thermal desorption spectroscopy experiments described in this thesis were performed in a vacuum chamber (a diagram of which can be found in figure 3.1) equipped with a sample manipulator, LEED, a quadrupole mass spectrometer, leak valves for dosing and for Ar sputtering, a turbo-molecular pump, a rotary pump, a titanium sorption pump, and a gate valve for isolating the chamber from the pumping system. This equipment is mounted on conflat flanges sealed with oxygen-free copper gaskets. What might best be termed the control system comprises all the support equipment that is used for the operation and monitoring of the chamber, and for the recording of measurements. This includes a temperature controller for the sample, the LEED power supply and controller, the mass spectrometer control, an ion pressure gauge and its supply, vernier manual positioner for the sample manipulator, and a 486 33MHz computer equipped with a data acquisition board.

The electrical connections between "outside and inside" the chamber are made through metal contacts fed through ceramic insulators.

In the chamber, we manage to maintain a base pressure in the mid 10^{-11} Torr range. This is accomplished by the use of the turbo-molecular pump backed by the rotary pump, with additional pumping provided by the titanium sorption pump. The turbo-

molecular pump is rated with a pumping speed of 200 L/s over most of the pressure range below 10^{-4} Torr. The rotary pump is turned on only occasionally between experimentation runs, but is left on during the actual experimentation to prevent buildup of the dosing and desorption products in the tube connecting the turbo-molecular pump to the rotary pump. Such a buildup could entail a loss of effectiveness of the turbo-molecular pump due to its maximum compression ratio.

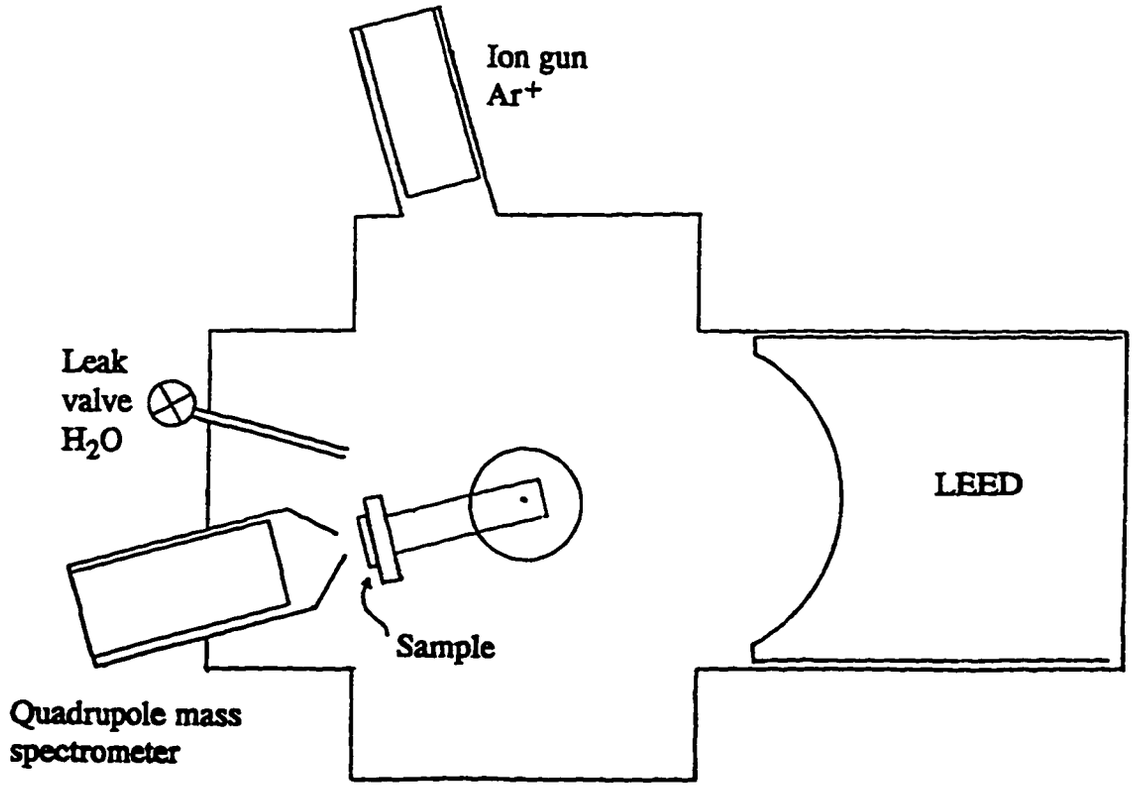

Fig. 3.1 Diagram of the TDS vacuum chamber.

The titanium evaporated onto the chamber walls that acts as our sorption pump, is evaporated in a section of the chamber away from the rest of the equipment so that the evaporation source is not in the line of sight of the sample or any of the measuring

equipment. This is a precaution to protect the other systems, but also to assure that the sample is in no risk of being contaminated by the evaporating Ti.

The ultra high vacuum is required to keep the sample clean and free of contaminants for a reasonable length of time, that is, at least as long as the total preparation and experimentation time required for one measurement run. Even at 1×10^{-10} Torr, assuming unity sticking coefficient, it would take only six hours to deposit one monolayer onto our sample. At the same pressure, it would only take about four minutes to contaminate an experiment with 1% of a monolayer, but at about 3×10^{-11} Torr, this 1% contamination would require more than twelve minutes.

To reach ultra high vacuum pressures, pumping alone is not usually sufficient; it is preferable to heat, or bakeout, the vacuum chamber to accelerate the outgassing of materials deposited on the chamber walls and all the equipment during the last contact with atmospheric pressures.

After a long series of measurements, as the sample and sample manipulator are allowed to entirely warm up, the pressure in the vacuum chamber will be seen to rise in bursts up to a few orders of magnitude higher than base pressure due to the evaporation of the condensate formed on the sample manipulator (during cooling the sample manipulator acts as a cold trap). After these transient pressure bursts the chamber pressure always returns to the 10^{-11} Torr range; this is so even after sputtering (due to the high purity of the Ar supply), and between each adsorption/desorption run during a given series of measurements.

The main pressure gauge on the system is a Bayard-Alpert type ionization gauge; it is a nude tube gauge, degassable by electron bombardment. Pressure readings can also be made using the total pressure setting on the mass spectrometer, but because of outgassing and conductance considerations the ionization gauge gives a better evaluation

of the chamber pressure, and furthermore, at ultra high vacuum pressures, the type of current measurement and the geometry of the Bayard-Alpert gauge minimize the background current measurement (c.f. the X-ray limit). Basically a Bayard-Alpert gauge consists of a collector surrounded by a cylindrical accelerating mesh, and a filament just outside of the mesh. The filament thermally emits electrons which are subsequently accelerated by the mesh. In the volume surrounded by the cylindrical mesh, the electrons ionize the gas. The positive ions are collected at the negative collector.

The gauge tube current measurement is converted in nitrogen equivalent pressure in the following manner: $P=K\times$(positive ion current to collector)/(electron emission current from filament to grid), where K is the gas sensitivity constant. Due to the variation of ionization cross section from gas to gas, the gauge sensitivity to gases relative to N_2, that is K_{gas}/K_{N_2}, can vary by a factor as large as almost 4 (e.g. $K_{Hg}/K_{N_2} = 3.64$). Conveniently, most of the gases used in our experiments are sensed with relative sensitivities close to 1: $K_{O_2}/K_{N_2} = 1.01$, $K_{H_2O}/K_{N_2} = 1.12$, $K_{Ar}/K_{N_2} = 1.29$, and $K_{CO_2}/K_{N_2} = 1.42$.

The X-ray limit for this nude tube type of ionization gauge is 2×10^{-11} Torr. Furthermore, these gauges are listed as being accurate to within roughly 20% because of variations in electrode structures. If the precise pressure measurements were to have been required, a calibration would have been performed.

3.2 Sample Preparation

3.2.1 Sample Mounting and Washing

The sample is mounted on a 0.5 mm thick molybdenum plate; it is held down by two clips made of 0.13 mm thick molybdenum. The sample plate is attached to the sample manipulator by a rigid stainless steel bracket. The sample plate is electrically grounded through an external connection, but isolated from the rest of the sample manipulator assembly; sample current measurements can be made through the external ground connection.

Whenever the sample has been extracted from the vacuum chamber and "manipulated" in atmosphere, including the first time it is prepared to be inserted into the chamber, it is important to confirm that no gross amounts of contaminants remain on the surface. These contaminants could include anything from dust to trace amounts of chemicals left on tools that might have inadvertently been improperly cleaned.

After the sample is mounted on its support plate, which is already attached to the manipulator, it is rinsed with generous amounts of solvents. Acetone or methanol are the usual choices, and more often than not, both are used in a series of repeated steps that minimize the residue left by either of the two solvents.

Any traces of solvents or other contaminants are removed during the bake-out of the chamber during the first steps of the pump down of the vacuum chamber. And of course, anything that might have survived these cleaning steps, would be removed during the first sputter and anneal of the sample.

3.2.2 Ar Sputter Gun

Just as it is important to keep our sample clean after preparation, it is essential to be able to remove any contaminants that might have "found their way" to the surface of the sample. After just two days, even at a base pressure of 3×10^{-11} Torr the sample has been exposed to 5 Langmuirs of possible contaminants. Before any experiment, the sample is therefore cleaned by sputtering with 500 eV Ar ions at a sample current of 10 μA for 30 minutes; this removes on the order of 10^2 atomic layers.

We use a Perkin Elmer model 14-161 2 kV Sputter Ion Gun that we control through a model 20-045 Sputter Ion Gun Control; a schematic representation of this system can be found in figure 3.2.

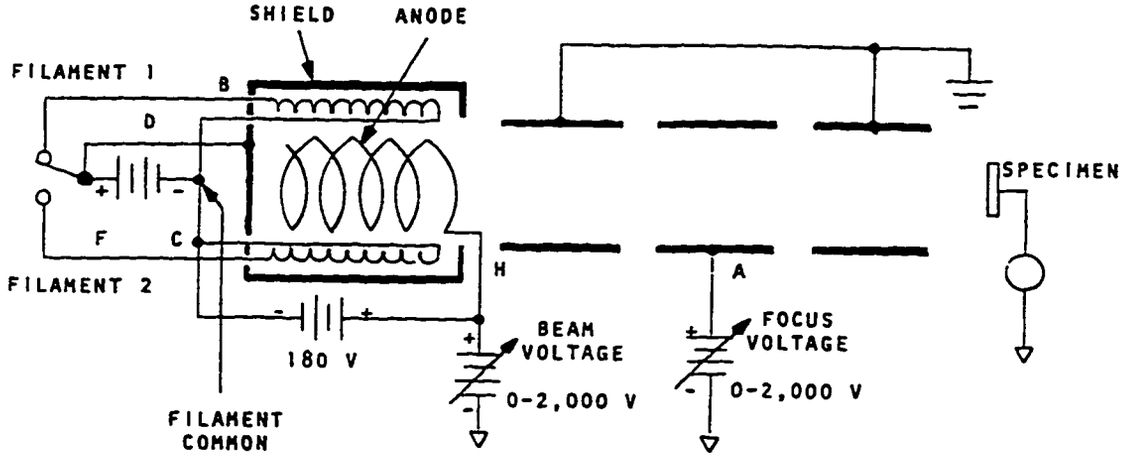

Fig. 3.2 Diagram of the ion sputter gun system including the sample [3.1].

The vacuum chamber is backfilled with Ar gas at a pressure of about 2×10^{-5} Torr, the ion gun is open and therefore the ionization chamber of the ion gun is also filled. A hot filament produces electrons which are then accelerated into the ionization chamber. The Ar ions produced in this fashion are then accelerated out of the gun by a potential

difference that is selected at the gun control. The gun is also equipped with a focusing lens to control the shape of the ion beam. The target, in this case the sample to be cleaned, is grounded to complete the electrical circuit and thus prevent sample charging.

3.2.3 Temperature Controller and Heater

After sputtering, the sample is annealed in vacuum at 840K for 10 minutes. This is to flatten the surface, restore long range order and get rid of the Ar imbedded during the sputtering process. The annealing is done by rapidly stepping up to the desired temperature. The same heater assembly is used as for the linear temperature ramp of the sample during the desorption process.

The heater element consists of a tungsten wire 0.2 mm in diameter and approximately 40 cm long. This wire is bent into a "flat spring" configuration and shielded with ceramic sheaths. Located behind the sample mounting plate, the heater is held in a box by a molybdenum belt. Its electrical resistance is about 0.8 Ω at room temperature, and increases considerably as it heats up as a current ≤ 2 amps is circulated through it.

Two chromel alumel thermocouples are glued close to the edges on the front surface of the sample. The glue is a zirconia based high temperature ceramic adhesive (Aremco 516). Both the chromel and alumel wires of both thermocouples have a diameter of 0.13 mm. Only one of these thermocouples was used to measure the

temperature of the sample surface during our desorption experiments, the other being used to evaluate possible gradients across the surface, and also as a back-up for the first.

The temperature during all steps of our experiments that required such control, was monitored and adjusted by a Eurotherm 818P Controller/Programmer operated in conjunction with a Eurocube 425 series thyristor unit by the same company. The system receives as input the voltage difference from a thermocouple, and outputs a modulated (by the thyristor) and rectified electrical current commensurate to the temperature increase the controller calculates is required to follow the temperature program. The feedback loop is maintained, and the system's temperature evolves toward a set point determined by the program entered in the controller. Series steps and linear ramps in temperature can be achieved with this system.

3.2.4 Cooling

Our sample is cooled by an open circuit of liquid nitrogen. By simple application of pressure in a cryogenic container, liquid nitrogen is made to flow through a tubing system that leads to a small rectangular copper container on the sample manipulator. A sapphire crystal (for electrical isolation) provides thermal contact between this bottle and a large cross section copper braid that reaches to the sample support plate.

With this nitrogen circuit we can cool our sample and provide a strong heat sink during heating cycles in order to limit the heating rate.

3.2.5 Doser

After our sample has been cooled to the desired temperature, it is turned to face the doser. The doser simply consists of a 4.8 mm internal diameter tube that leads from a gas leak valve into the chamber. To obtain a sufficiently even distribution of the dose across the surface, the sample is kept at about 1 cm from the tip of the doser.

Tests were performed to assess the effects of a possible range of coverages on the sample during a desorption run. We refer the reader to the discussion and analysis sections for details on the uniformity of the dose across the surface.

3.3 Surface Characterization

The surface preparation steps we have been describing modify the surface stoichiometry and structure, and can introduce foreign atomic species in the surface region: e.g. Ar imbedded during the sputtering process. Steps, as we have also described earlier, are taken to clean the surface of these contaminants and to restore the structure. It is essential that we verify to what degree these restoration procedures are successful.

Auger Electron Spectroscopy, AES is used to identify the atomic species present on the sample surface, and Low Energy Electron Diffraction and High Resolution LEED are used to study the surface structure.

3.3.1 Auger Electron Spectroscopy

The AES apparatus we used is from Perkin Elmer, and consists of a model 137 PC interface, a model 10-155 Cylindrical Mirror Analyzer (CMA), a model 11-010 5kV electron gun control, a model 32-100 electron multiplier power supply, a model 96A V/f preamplifier, and a model 32-150 digital analyzer control.

A schematic diagram of a CMA can be found in figure 3.3. The CMA is a system of electric lenses made of concentric cylinders. An electron gun sends a monoenergetic beam of electrons (~10^3 eV) onto a sample, and the CMA selects the energy of the returning electrons (less than the incident beam energy). Intensity spectra of the backscattered electrons are recorded and subsequently differentiated for analysis.

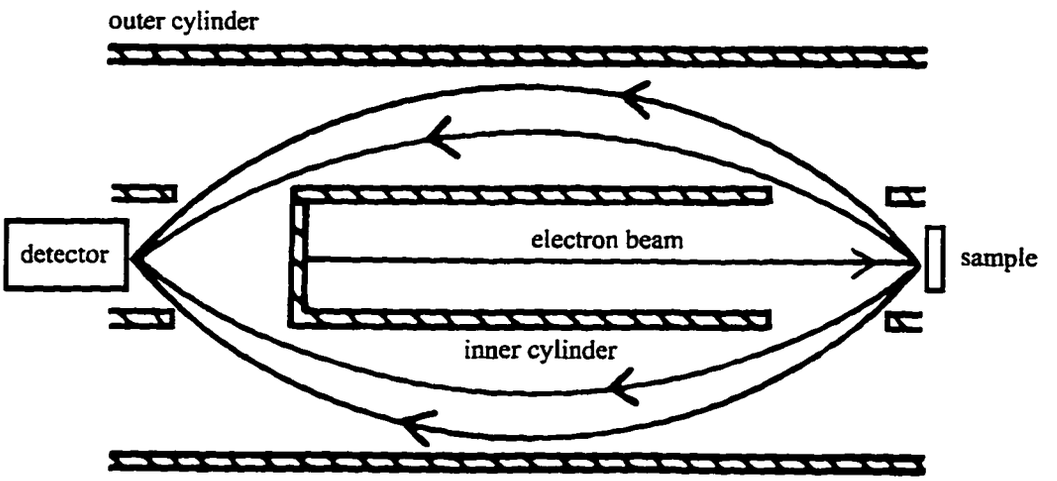

Fig. 3.3 Representation of a Cylindrical Mirror Analyzer with electron trajectories (this image has cylindrical symmetry about the horizontal axis) [2.3].

3.3.2 LEED and HRLEED

A schematic representation of the type of the LEED apparatus that is installed on the vacuum chamber used for our TDS measurements can be found in figure 3.4.

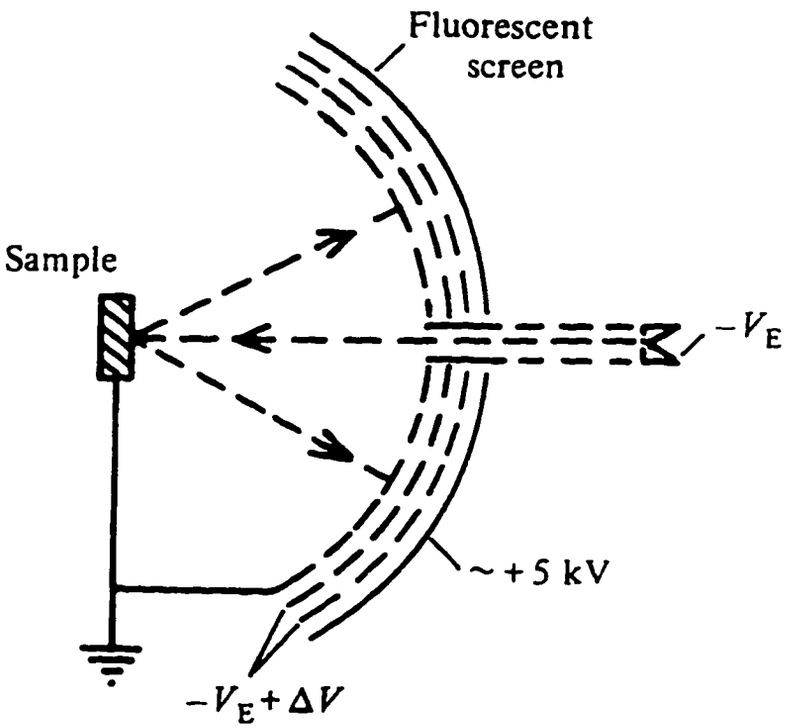

Fig. 3.4 Schematic diagram of display LEED 'optics. The potential V_E defines the electron energy as eV_E [2.3].

The electron gun provides an electron beam of monoenergetic electrons (10's to few 10^2 eV) of a focused diameter at the sample of the order of 1mm. A system of electrostatic lenses provides the focusing.

On a second chamber, in which more detailed surface characterization was carried out to test the effects of our "sample preparation recipes" (see chapter 4), there is another LEED apparatus. This one, in addition to being used as a direct viewing LEED device, can be operated in a high resolution mode. A system of electronic lenses guides the electron beam to the sample and back to a channeltron (an electron "multiplier" operating on a cascade process). The double system of octapolar lenses, as well as the general geometry of the system can be seen in figure 3.5.

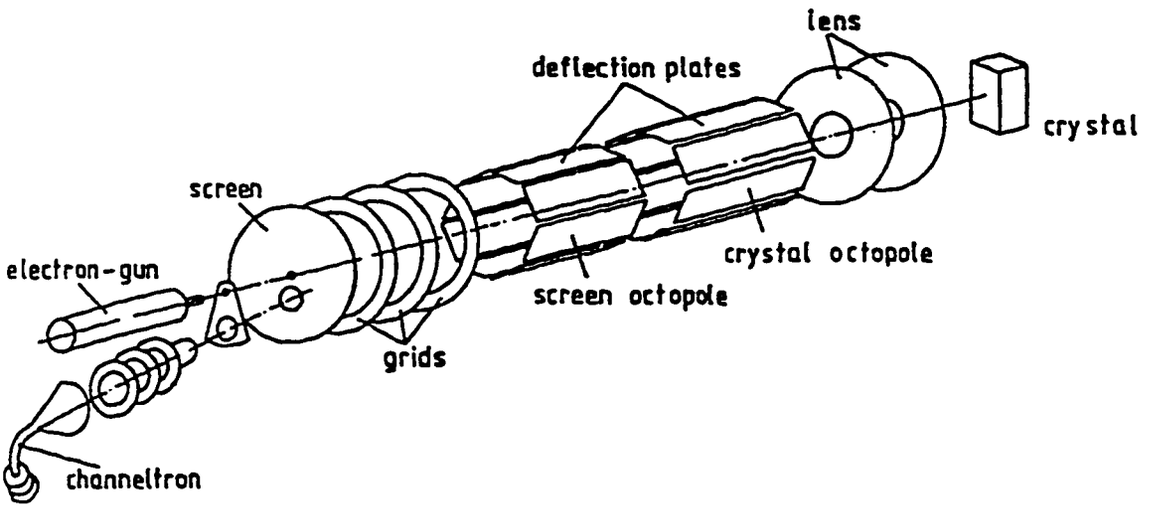

Fig. 3.5 Basic design of the HRLEED apparatus [3.2].

3.4 TDS: Measurement Acquisition

Ultimately the goal of the experimental procedure is to obtain the desorption curves, that is: desorption rate as a function of temperature. The sample surface

temperature is readily available through the thermocouples attached to the face of the sample. On the other hand, the desorption rate is not directly available, and must therefore be related to an easily measurable quantity.

We begin by considering the shroud placed around the QMS and write an equation representing the throughput into the shroud volume due to the desorption from the sample surface:

(desorption flux, Q_d) = (number of sites on the sample) × (desorption rate per site) (3.1)

$$Q_d = N_0 \cdot r_d, \tag{3.2}$$

and let: θ = coverage
S = pumping speed
P = pressure in the shroud

Now, if we relegate the contribution of any other source to the background (which we shall account for in the analysis), we can write by conservation of particles:

$$Q_d = \frac{PS}{kT_{ch}} + \frac{V}{kT_{ch}} \frac{dP}{dt}, \tag{3.3}$$

where, k is Boltzmann's constant, and T_{ch} is the temperature of the chamber. Next we consider the limit in which experimental times are much longer than the pumping time constant, that is:

$$\frac{P}{dP/dt} >> \frac{V}{S}, \tag{3.4}$$

we can assume steady state:

$$Q_d \cong P \cdot S, \tag{3.5}$$

or

$$-\frac{d\theta}{dt} = r_d = \frac{S}{N_0 \cdot kT_{ch}} P. \tag{3.6}$$

Simply put, the desorption rate is proportional to the pressure in the shroud.

Now that we can relate the desorption rate to a readily available physical quantity, we need only measure the partial pressure of mass 18 (for water), the sample temperature, and time. The temperature is measured by the temperature controller that we discussed in section 3.2.3, and the pressure is measured by a Quadrupole Mass Spectrometer which we shall discuss presently in section 3.4.1. Time is recorded from the internal clock of the 486 33MHz computer that was mentioned in section 3.1.

3.4.1 Mass Spectrometer

To measure the partial pressures of the various gases of interest, to study the background levels of gasses present in the chamber, and to test for leaks, we used a radio frequency quadrupole mass spectrometer: Selectorr from Spectramass. This device can be broken up into three major components: the ionization region, the quadrupole mass selector, and an ion detector. In the ionization region, the gasses present are ionized by electron bombardment and the positive ions are accelerated toward the quadrupole array. By properly adjusting the voltages applied to the two diagonally coupled pairs of rods that make up the quadrupole, the desired ratio of charge to mass can be selected. The selected ions are detected at a channeltron, where by impact the ions generate a cascade of electrons that is then fed to an amplification circuit and the control unit.

The shroud in which the mass spectrometer is encased serves to increase selectivity. It was used in the experiments with H_2O, but was originally designed for CO_2 adsorption/desorption experiments. The pumping time constant of the shroud was increased by reducing its aperture conductance, but it still remained at least one order of magnitude smaller than the experiment times as discussed in the introductory portion of

section 3.4. Such an increase in time constant results in an amplified pressure rise in the shroud; this compensates for the loss of signal associated with selectivity, and would serve to amplify the low signals for CO_2 desorption. The shroud was optimized for rare gas pumping, and some possible adverse effects of the shroud on the H_2O TDS will be discussed in chapter 5.

The diameter of the shroud aperture is approximately 6 mm. For the desorption measurements, the sample is brought to a distance of 2 to 3 mm from the opening in the shroud. In this way, H_2O or background gasses that might desorb or outgas from other regions than the sample are shielded from the line of sight into the shroud. This also reduces the 11 mm diameter of the sample to a slightly smaller effective area.

3.4.2 Data Acquisition

As stated earlier, to obtain the desorption curves, we must record as a function of time both the partial pressure for mass 18 and the sample surface temperature. From these quantities, we can graph the desorption rate as a function of temperature, and calculate the various integrals over time that will be required (see chapter 5).

The surface temperature measured by one of the thermocouples attached to the sample is recorded from the ASCII output of the temperature controller (section 3.2.3) in RS232 protocol. The desorption rate, in the form of the mass 18 partial pressure from the quadrupole mass spectrometer is available from the QMS control unit as an analog voltage output.

The final piece of equipment involved in the measurements is the 486 33MHz PC. The ASCII string representing the temperature is read through one of the serial ports of the PC, and the partial pressure is read by a National Instruments Data AcQuisition board (model AT-MIO-16) at an analog to digital port on a scale of +10 V to -10 V with 12 bits.

Using the LabWindows package that was purchased with the NIDAQ board, and a QuickBasic 4.5 compiler, we wrote a data acquisition program that reads and then records on the PC's hard drive, both the sample temperature and the water partial pressure. This program prompts the experimenter for the start and end temperatures of each desorption run, the temperature increments at which measurements should be recorded, an approximate temperature ramp rate (simply the same rate as that programmed into the temperature controller), and the pressure scale on the QMS control unit (for later referral). The program is designed to evaluate early in a desorption run how fast in time the temperature increments are actually occurring and, from that, to determine the maximum number of times a given measurement can be repeated and averaged for each increment without missing the next increment; this acts as a "digital time constant" to improve signal to noise ratio. Each of these measured points (one for each increment after averaging) is accompanied by the clock time on the PC just before and just after the repeated measurements.

The data acquisition program can be found in Appendix A.

CHAPTER 4
SURFACE CHARACTERIZATION: MEASUREMENTS AND ANALYSIS

4.1 Introduction

Before the actual Thermal Desorption Measurements can be performed, the sample must be cleaned. This preparation includes both sputtering and annealing. Subsequently, as mentioned in chapter 3, it is necessary to verify that the sample surface has been returned to its normal (1×1) surface structure and stoichiometry. A complete and detailed list of the preparation steps can be found in Appendix B.

In this chapter we present and analyze the measurements made in the examination of the sample surface.

4.2 Redhead Method

In 1962, Dr. P. A. Redhead of the Radio and Electrical Engineering Division of the National Research Council, an important figure in the field of adsorption/desorption, proposed a method for analyzing thermal desorption spectra[4.1]. This method is based

on a variation of the heating rates, and the aspect of it that is of interest to us, is that it allows for the determination of the activation energy without assuming a value for the exponential prefactor in the Arrhenius form.

The Arrhenius form for first order kinetics, as described in chapter 2, is used, and it is assumed that the desorption energy is independent of coverage:

$$\dot{\theta} = -\nu\theta\, e^{-E/kT} \tag{4.1}$$

In the case of a linear temperature ramp:

$$T(t) = T_0 + \beta\, t \quad , \qquad \frac{dT}{dt} = \beta \tag{4.2}$$

it is possible to solve by differentiation for the temperature T_p at which the desorption rate peaks:

$$\frac{d\dot{\theta}}{dT} = -\,n\frac{d\theta}{dt}\frac{dt}{dT}e^{-E/kT} - \nu\theta\frac{E}{kT^2}e^{-E/kT} \tag{4.3}$$

$$\frac{d\dot{\theta}}{dT} = -\,\frac{\nu\dot{\theta}}{\beta}e^{-E/kT} + \dot{\theta}\frac{E}{kT^2} \tag{4.4}$$

At T_p we can set the right hand side equal to zero and cancel out $\dot{\theta}$, so that we get:

$$\frac{E}{kT_p^2} = \frac{\nu}{\beta}e^{-E/kT_p} \tag{4.5}$$

Now, by repeating the same desorption experiment for a variety of heating rates, one can evaluate the energy of desorption by plotting $\ln T_p$ versus $\ln\beta$:

$$\frac{E}{kT_p} = \frac{d\ln\beta}{d\ln T_p} - 2 \tag{4.6}$$

We used this method to perform a rough evaluation of the energy of desorption of Ar embedded during sputtering. We performed measurements of Ar "desorption" with our TDS setup as a first step in creating a "recipe" for producing a high step density (poorly annealed) surface for comparative TDS measurements. Due to the developments of our analysis of our TDS measurements on the well annealed surface, we have postponed these comparative measurements to a later date; nevertheless the Redhead method is included here (as are the Ar measurements) because it represents a valid methodology in the field of desorption kinetics.

The assumptions of first order kinetics and coverage independent desorption energy are not related to any physical intuition, very simply they are made for the sake of simplicity. We were not interested in studying the physics of the desorption of embedded argon in any detail, rather, we were interested in finding a "ballpark" value for the energy of desorption.

4.3 Sputtering and Annealing

During the sputtering process, some Ar is implanted in the surface region of the sample being "cleaned". The annealing process therefore serves two purposes: first, it allows for the reconstruction of the surface layers, and second, it activates the desorption of the implanted atoms. Of course, these two processes occur simultaneously and are interrelated.

From the recorded TDS like spectra of the "desorption" of the embedded Ar, we observed that at temperatures higher than 820K, no more Ar is detected leaving the surface.

In two separate instances, we sputtered our sample for an integrated current of $10\,\mu A \times 10$ min. We then heated the sample with two different heating rates: $\beta_1 = 0.1$ K/s and $\beta_2 = 1$ K/s. We recorded the partial pressure of Ar in the QMS shroud and sample temperature as a function of time as in our normal TDS procedure, and obtained the two curves found in figure 4.1.

As stated earlier, we used the Redhead method to analyze this data. We performed the TDS measurements with only two different heating rates, and therefore dispense with the graph of $\ln T_p$ versus $\ln\beta$ as it would contain only two points, (0.1 K/s, 730K) and (1 K/s, 780K) with $\Delta T_p = \pm 5$K. Looking at the final equation in the previous section, it is obvious that the slope of $d\ln\beta/d\ln T_p$ ought not be linear if one expects to find the same value for E at various T_p's. And yet, we can assume nothing more than linearity between the two points we have. We therefore proceeded in the following manner:

$$\frac{E_i}{k\,T_{p_i}} = \frac{\left(\ln\beta_j - \ln\beta_k\right)}{\left(\ln T_{p_j} - \ln T_{p_k}\right)} - 2 \qquad (4.7)$$

where for T_{p_i} we took the average of T_{p_j} and T_{p_k}, and took $\Delta(\ln T_{p_j} - \ln T_{p_k})$ as the dominant uncertainty.

We therefore believe that the desorption energy for embedded Ar in the TiO_2 (110) surface is about (2.1 ± 0.4) eV.

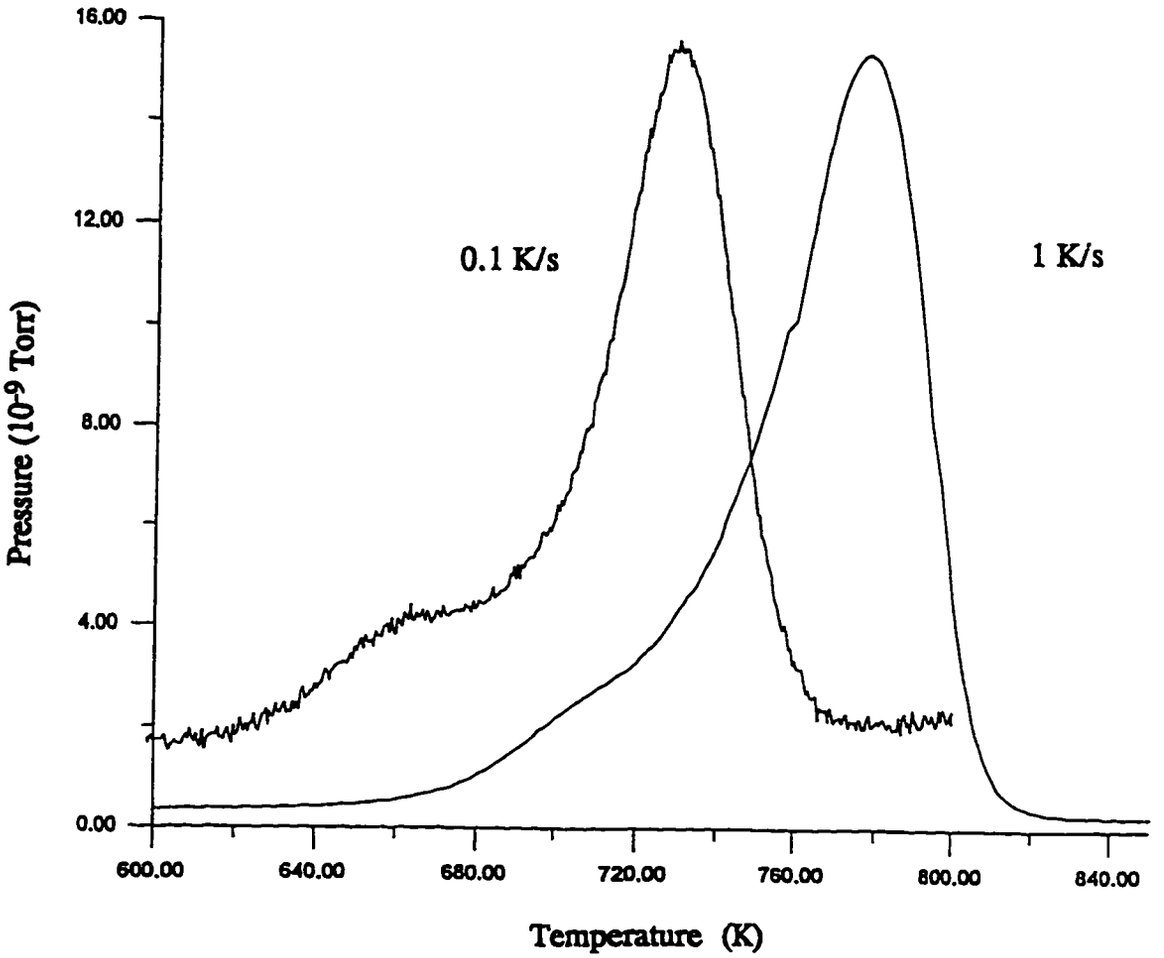

Fig. 4.1 TDS of embedded Ar at 0.1 K/s and 1 K/s. The 0.1 K/s run has been multiplied by ~ 3 for comparison.

4.4 Auger Electron Spectroscopy

On another TiO_2 (110) sample in a second vacuum chamber, we performed AES measurements. We did this to assure ourselves of the cleanness and stoichiometry of the TiO_2 (110) surface after our surface preparation recipe.

It was first necessary to calibrate the thermocouple temperature measurements from one sample to the other. We performed the same two desorption runs for embedded Ar (in the second chamber, with the second sample), and from these (and the T peak positions from the same experiment in the first chamber with the first sample) obtained two different sets of peak positions:

chamber 1: (1 K/s,745K) and (0.1 K/s,700K)

chamber 2: (1 K/s,778K) and (0.1 K/s,729K)

From these numbers we deduced that a 30K shift was sufficient to compare temperatures measured on the two chambers in the neighborhood of the anneal and Ar desorption temperatures.

We then proceeded to sputter and anneal this sample according to the same recipe followed for the sample on which the TDS measurements were being taken. The AES probing revealed that the surface was near stoichiometric, and that essentially no Ar remained (no more than 0.5%, and hidden by the noise).

The preparation of the high step density surface, annealing at 710K for 60 minutes produced similar (qualitatively indistinguishable) results in terms of Ar depletion.

4.5 LEED and HRLEED

Both chambers being equipped with Low Energy Electron Diffraction apparatus, the surface structures could readily be compared. The LEED device on the chamber equipped with the Auger Electron Spectrometer is also designed to perform HRLEED measurements.

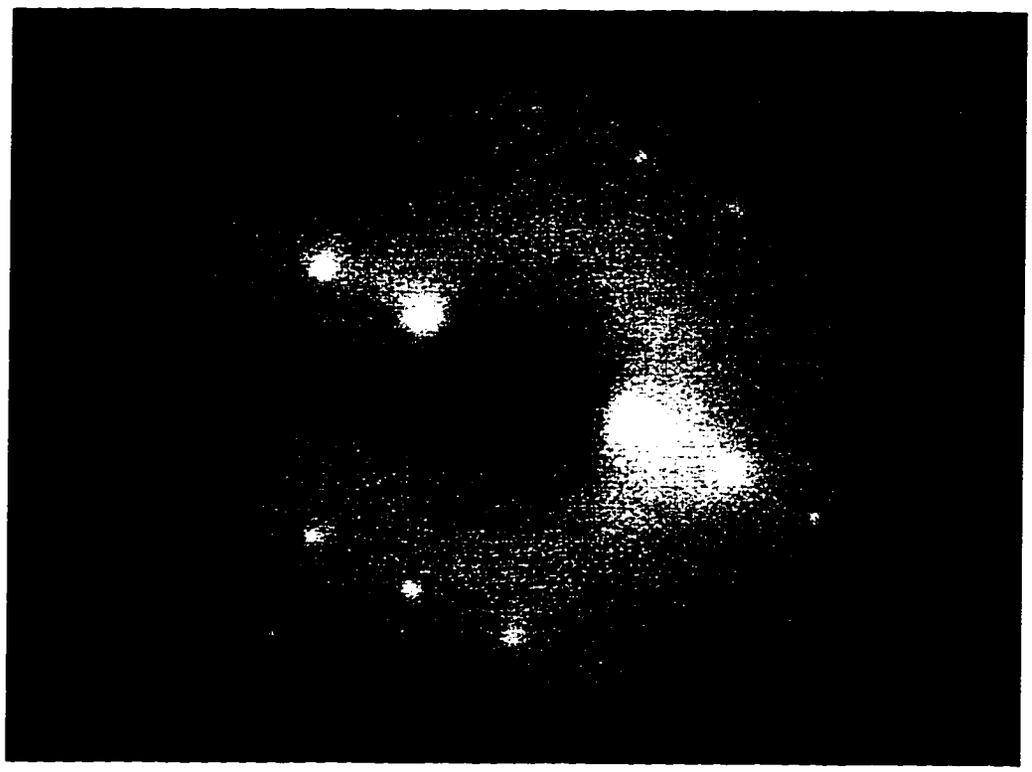

Fig. 4.2 Picture from the rearview LEED on the TDS chamber. Compare to fig. 1.2.

Looking at the LEED pattern produced by our sample (see figure 4.2). We recognize the familiar pattern of the (1×1) (110) surface structure for TiO_2 (compare to

figure 1.2). Furthermore the reciprocal lattice parameters are consistent, as checked by the ratio of spot distances in both axial directions in the diffraction patterns, with the accepted values. Also, based on a few "spot checks" with LEED, we surmise that the surface preparation recipe followed before each of our runs of TDS measurements did not produce any noticeable reconstruction.

Again relying on the chamber to chamber temperature calibration, we followed the recipe for the high step density surface and proceeded to scan the surface lattice in HRLEED, the recorded scans can be found in figure 4.3. The presence of the sharp (delta function like) peak confirms the restoration of long range (1×1) order. From the full width at half maximum of the second (wider) component of the peak that can be found on out of phase (see chapter 2, section 2.2.3) scans such as these, we can evaluate the mean width of terraces to be ~ 50 Å. This represents a surface step density of approximately 20%, that is, 20% of unit cells are at step edges. Such terraces populating this surface contain approximately 15 unit cells in one direction, and about 7 in the other. (The calculations can be found in Appendix C)

We evaluate the mean width of flat terraces on our low step density surface based on the study performed with the same equipment on a TiO_2 (110) surface by Bruno Grossmann and Peter Piercy[4.2]. The surface preparation recipe they followed involved sputtering for an integrated current of 300 μA·min, and after 10 minutes at 800K (the temperature in that study closest to our 840K–30K) they found a mean terrace width of 100 Å. After sputtering for an integrated current of 300 μA·min, but annealing at 810K for 10 minutes, as in the recipe for our low step density surface, the mean terrace width should be equal to or slightly greater than 100 Å. This means a surface step density smaller than 10%.

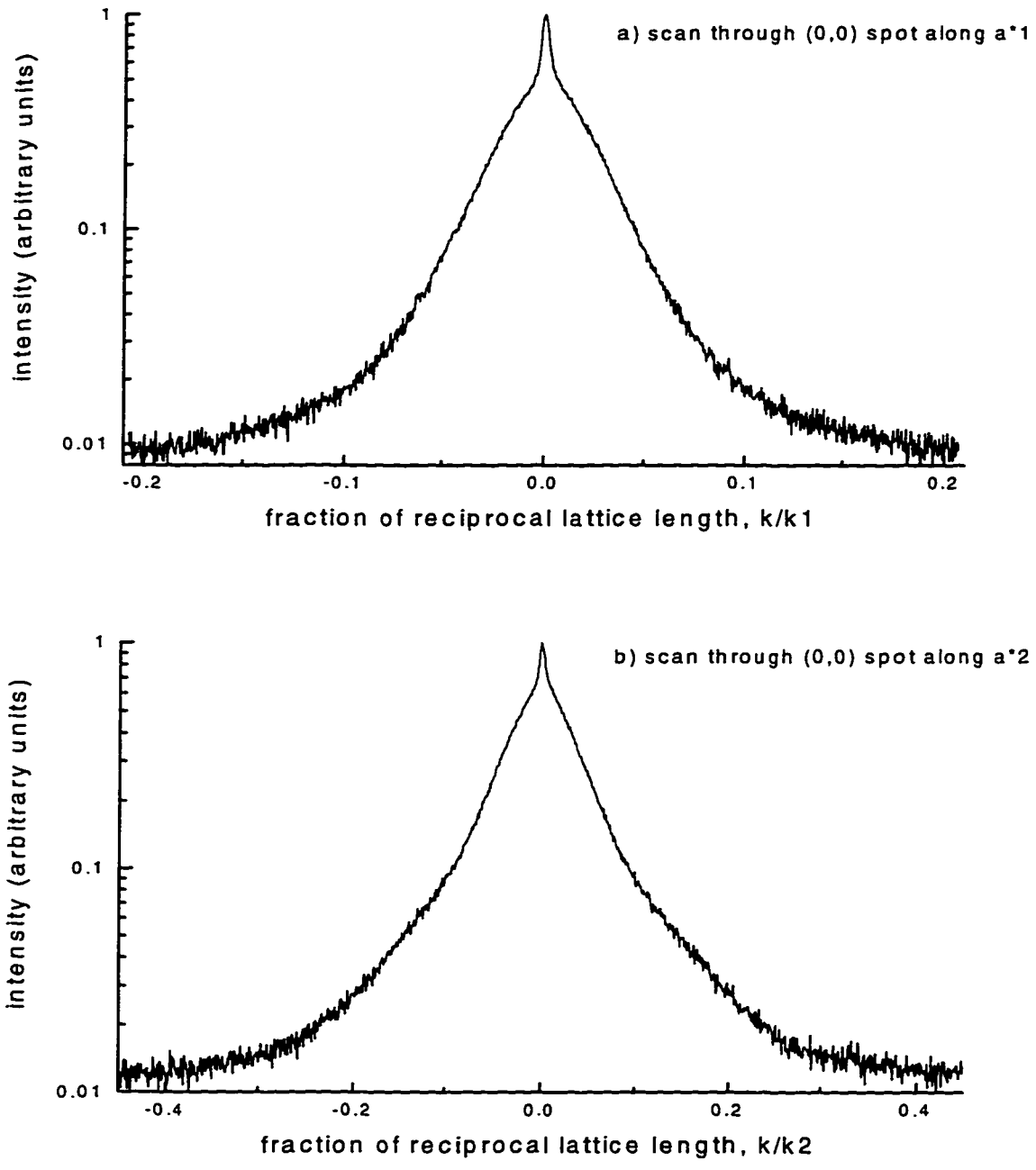

Fig. 4.3 Out of phase HRLEED scans on the high step density surface. The intensity axes are scaled to the height of the second wider component of the peaks The directions can be identified by referring to fig. 1.2. Note the difference of x-axis between 4.3.a and 4.3.b.

CHAPTER 5
WATER THERMAL DESORPTION: MEASUREMENTS AND ANALYSIS

5.1 Introduction

After the surface has been prepared in a fashion that restores the normal TiO_2 (110) (1×1) stoichiometry and structure, we are ready to perform the thermal desorption measurements. The procedure involves cooling the sample to $T < 110K$, exposing it to water, and then recording the partial pressure of water and the sample temperature as the sample is linearly ramped in temperature. A complete and detailed list of the adsorption/desorption experimental steps can be found in Appendix B.

In this chapter we present and analyze the thermal desorption measurements made in our study of the H_2O / TiO_2 (110) (1×1) system.

5.2 Coverage Calibration

In chapter 3, Experimental Setup and Method, we explained that the quantities measured in the laboratory are the partial pressure of the desorbing H_2O gas, the TiO_2 sample surface temperature, and the adsorption dose. We did not perform a calibration of the dosing procedure and therefore do not have a precise measurement of this quantity, instead we have a reading of the vacuum chamber pressure before we turned the sample to face the doser and the time spent by the sample facing the doser; to within a constant this is equal to the amount dosed. A calibration could be performed using the following equation: $coverage = D \cdot S = g \cdot K \cdot S \cdot (P_{H_2O} \cdot t)$; g would relate the pressure at the doser to the pressure at the chamber pressure gauge (affected by the pumping, including the adsorption on the chamber walls), K would convert the pressure into a number of impacts on the sample, and S, the sticking coefficient, would account for the factors described in chapter 2. The interest in evaluating the dose would be to determine the sticking coefficient; this was not one of the goals of our experiment, instead we shall work with a relative calibration of initial coverage as described in chapter 1, and use a ratio of integrated area of the desorption curves as our measure of relative coverage.

We should note, at this point, that this coverage calibration gives the surface density of the adsorbate in terms of occupation of the available sites, and not in terms of sample area. Our coverage of 1 ML therefore represents one adsorbed particle per site as opposed to a certain number of particles per square centimeter.

To begin our analysis, we therefore have desorption curves described by arrays of points $(T(t), P(t))$, and we recall that equation (3.6) relates the desorption rate to the pressure:

$$\dot{\theta} = -\frac{S}{N_0 \cdot kT_{ch}} P \quad or \quad simply \quad \dot{\theta} = -C \cdot P \tag{5.1}$$

We evaluate the initial coverage for each desorption curve:

$$\theta_0 = \int_0^\infty dt \left|\dot{\theta}\right| \tag{5.2}$$

and from this we determine the calibration constant C using the saturated 310K-260K desorption peak. We define $\theta = 1$ ML as the saturation area of the 310K-260K peak. We can also determine the depletion as a function of time:

$$\delta(t) = \theta_0 - \int_t^\infty dt' \left|\dot{\theta}\right| \tag{5.3}$$

Finally, since we have $T(t)$, we can rewrite all these equations as functions of sample surface temperature. Moreover, since we used a temperature ramp of 1 K/s, integrals over time and over temperature have the same numerical value, but naturally have their respective units.

As an activated process, desorption can be parametrized by an Arrhenius form. We therefore take as kinetic ansatz, as discussed in chapter 2, the Arrhenius formula:

$$\dot{\theta} = - \nu_{eff} \cdot e^{-E/kT} \tag{5.4}$$

where: E is the desorption activation energy

ν_{eff} is the effective prefactor with units s^{-1}

Both ν_{eff} and E can be coverage dependent.

Before we can apply these equations to our measurements, it is important to consider the pressure background in the shroud of our QMS. Specific sources of background will be discussed in section 5.5, but at this point we shall leave it to say that our curve fits or data treatments will be done on sufficiently short temperature (time) ranges that the background can be taken to be linear.

5.3 Measurements

Before we could determine a reasonable coverage calibration, we first performed a background subtraction. We looked at the lowest possible coverage file that we recorded, that is, a desorption run not preceded by water dosing. This file could readily be fit to a slowly (as compared to the curvature of a desorption peak) increasing exponential. The shape of the background that we determined was:

$$B(t) = B_0 + B_1 \cdot e^{b_1 T} \tag{5.5}$$

We kept the same curvature b_1 for all the background subtractions and allowed the additive and multiplicative factors B_0 and B_1 to vary from curve to curve. We took as an evaluation of uncertainty on this background, half the difference of the integrated areas before and after subtraction of the exponential background, neglecting the B_0 offset. These uncertainties are listed in table 5.1, and the set of pressure versus temperature curves that we obtained can be found in figure 5.1. We label the peak at 310-260K peak 1, the peak at 175K peak 2, and the peak at 150K peak 3.

The reader may note that the units of the ordinate in figure 5.1 is pressure, that is to say, that the curves have not been scaled to reflect our coverage calibration of 1 ML for the file just prior to the appearance of the second peak. Assuming that the first site population reaches unity coverage between the eighth and ninth highest coverage files in figure 5.1 (and table 5.1), we get a calibration constant of C^{-1} = 15.04 Torr×s/ML. Therefore all the pressures must be multiplied by C to convert them into the units of rate of coverage variation. We list the integrated areas, and the relative uncertainties due to the background subtraction in order of increasing coverage in table 5.1. There is unfortunately no uncumbersome way of explicitly relating each of the curves in figure 5.1 to the numbers in table 5.1, but the reader may note that the curves can readily be identified in order of increasing coverage visually.

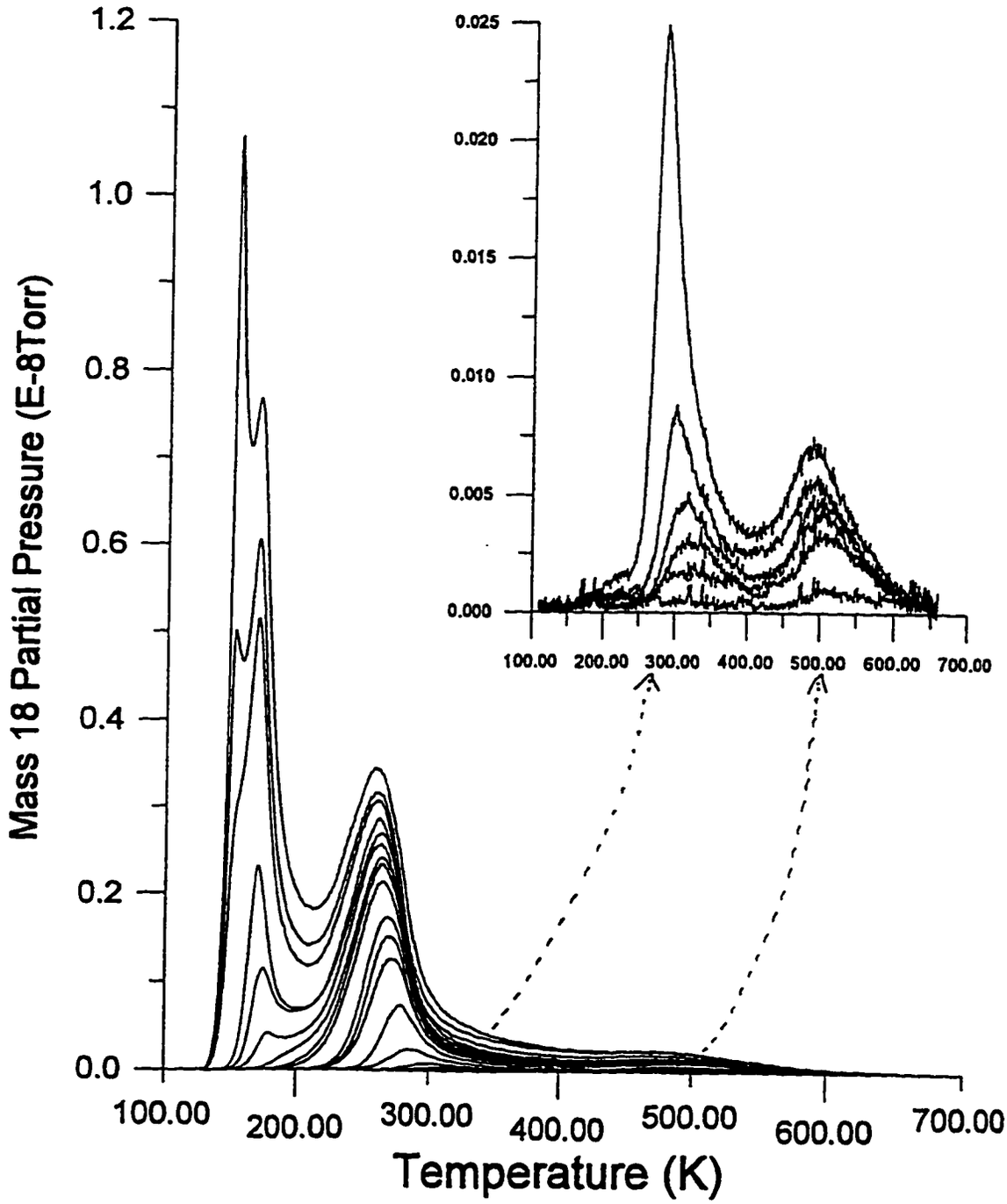

Fig. 5.1 This is the complete set of desorption curves after background subtraction. In all, there are 19 curves in this figure. The smaller, inset graph is an enlargement of the 6 lower initial coverage curves on the main graph. Counting the curves from higher to lower area at the 310K-260K peak on the main graph, the 14^{th} curve is the first (largest area) curve in the inset. The 17 higher coverage curves were analyzed, and are listed in table 5.1. (The lowest 2 curves in the inset could not be analyzed due to a poor signal to noise ratio.)

Table 5.1 All the data pertinent to the analysis of each file: the total calibrated initial coverage, the uncertainty on the coverage, the un-calibrated curve area, the fraction of peak height up to which the fit was performed, the P_0 and P_1 parameters for equation (5.11), and the Arrhenius parameters. The ν_{eff} are converted (see section 5.4.2). The area of the peak at 500K (0.5 Torr·s ± 0.1 Torr·s) was subtracted from the un-calibrated curve areas before they were divided to give the calibrated coverages in units of monolayers.

θ	Δθ	desorption curve area	fit fraction of peak	P_0	P_1	E	ν_{eff}
ML	ML	Torr·s	1/#	10^{-3} Torr	10^{-6} Torr/s	eV	s^{-1}
0.03	0.04	0.83	4	-8.51	2.65	0.55	3.9×10^{5}
0.05	0.04	1.03	4	-8.74	2.30	0.69	2.6×10^{8}
0.07	0.03	1.44	4	-9.04	8.23	0.87	1.1×10^{12}
0.15	0.03	2.56	4	-8.30	13.9	0.82	2.2×10^{12}
"	"	"	16	-8.30	14.0	0.90	1.1×10^{14}
0.31	0.05	5.00	4	-8.76	8.77	0.80	6.1×10^{12}
0.53	0.08	8.28	4	-8.51	15.2	0.55	3.7×10^{8}
0.61	0.06	9.34	4	.7.27	12.1	0.56	1.1×10^{9}
0.71	0.05	10.83	4	-8.30	14.2	0.57	2.6×10^{9}
"	"	"	32	-8.37	16.2	0.58	3.9×10^{9}
0.96	0.06	14.48	32	-8.47	12.4	0.50	6.2×10^{8}
1.04	0.06	15.62	32	-7.44	10.9	0.43	3.7×10^{7}
1.17	0.07	17.64	32	-7.66	20.8	0.38	1.8×10^{7}
1.31	0.07	19.56	4	-6.51	16.0	0.39	4.1×10^{8}
1.62	0.07	24.01	4	-7.30	25.0	0.49	2.5×10^{12}
1.75	0.06	25.99	4	-7.29	0, fixed	0.47	2.5×10^{12}
2.82	0.06	41.42	4	-7.43	0, fixed	0.49	8.5×10^{14}
3.40	0.09	49.78	4	-7.63	0, fixed	0.48	6.2×10^{14}
"	"	"	16	-7.49	0, fixed	0.50	3.7×10^{15}
4.38	0.09	63.99	4	-7.25	0, fixed	0.47	4.9×10^{14}

A second way of presenting this data that allows for a good understanding of what is happening on the surface of the sample is to plot the depletion as a function of temperature. A so called depletion graph, like the one found in figure 5.2, is the first step in an isosteric analysis, which we shall explain presently.

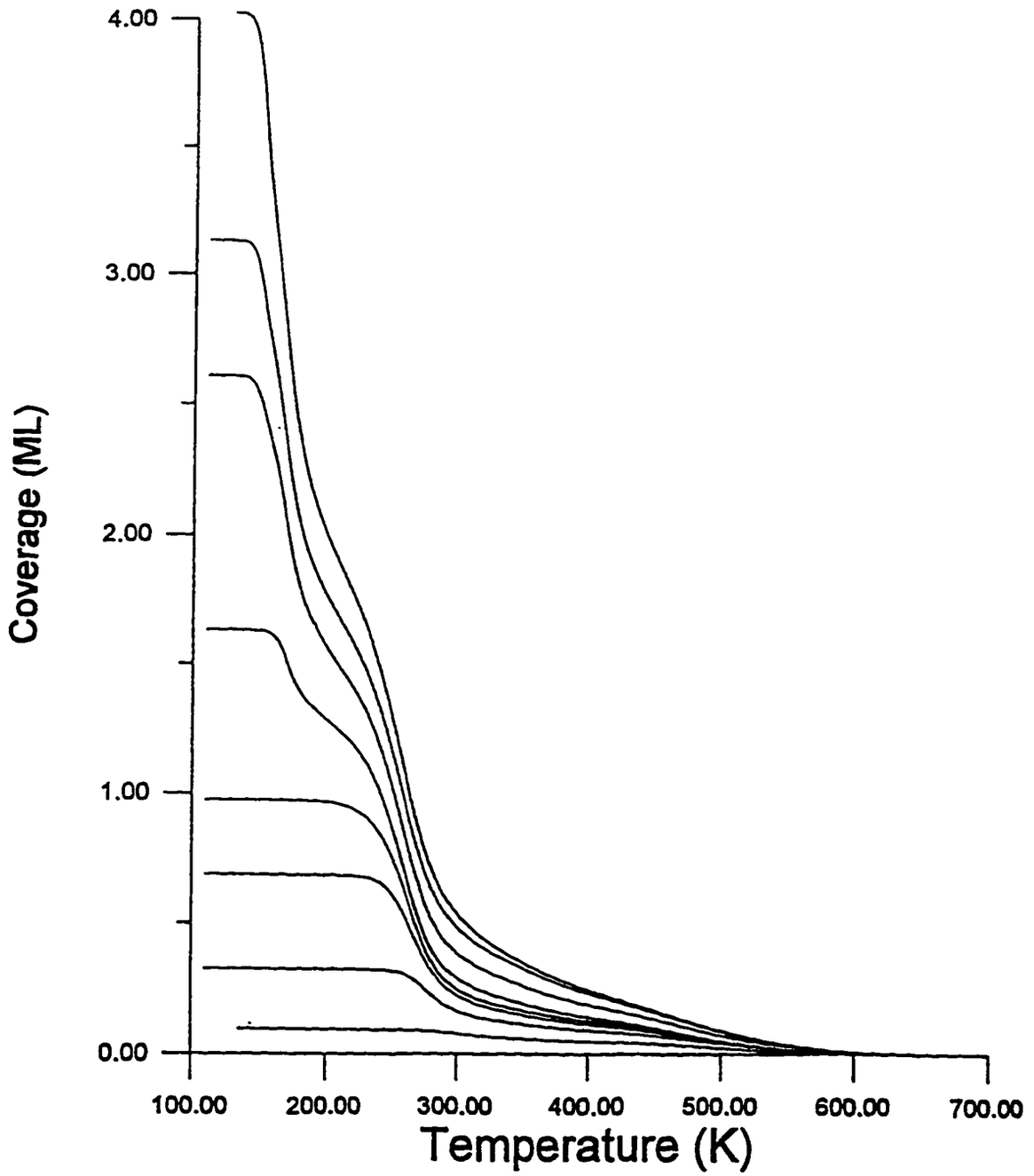

Fig. 5.2 This is the complete set of depletion curves using equation (5.3) (from the desorption curves after background subtraction).

5.3.1 Preliminary Analysis

A common approach to the analysis of desorption curves is the isosteric method. This is a full peak method in that it utilizes the entire curve of each peak for determining the Arrhenius parameters. Technically, the isosteric analysis requires finding the $(\dot{\theta},T)$ points at equal values of coverage for the set of desorption curves. To do this, a series of horizontal lines can be imagined cutting across figure 5.2. The series of $(\dot{\theta},T)$ points from figure 5.1 associated with each of the (θ,T) intersections of one of these horizontal lines forms an isostere, that is, a desorption rate versus temperature curve at constant coverage.

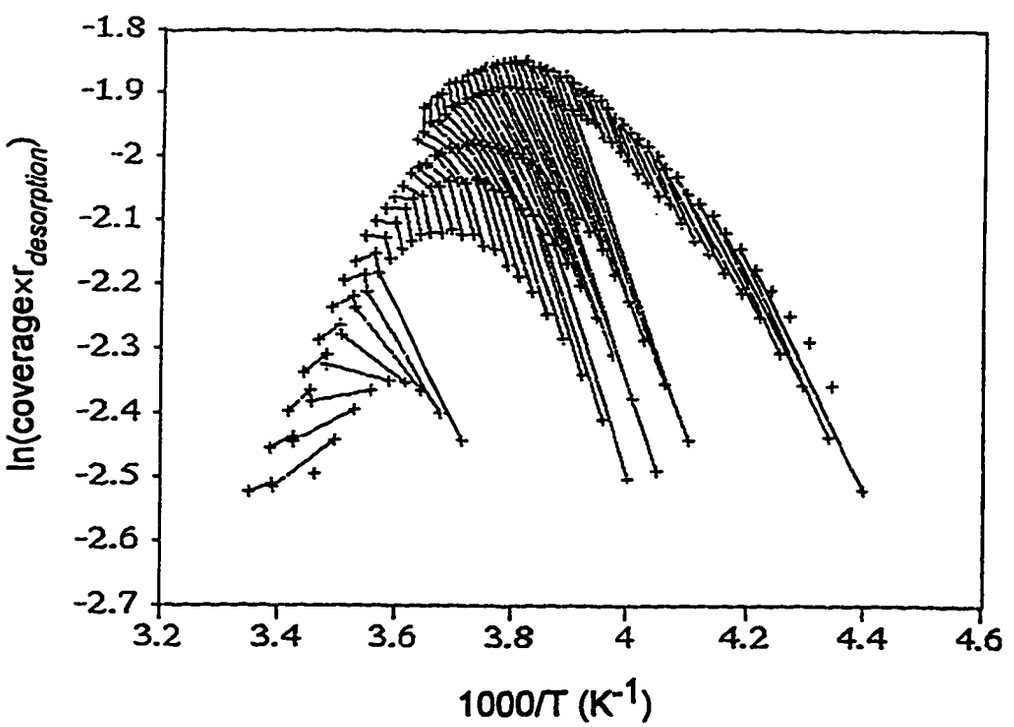

Fig. 5.3 Isosteres for the determination of the Arrhenius parameters for peak 1, obtained with Astek [5.1]. High temperatures are associated with small fractions of initial coverage remaining.

In figure 5.3, the isosteres are plotted as ln(coverage×desorption rate) versus the inverse of sample surface temperature; the multiplication of the desorption rate by the coverage value for each isostere serves to visually separate the isosteres on the graph. Looking at the Arrhenius form, equation 5.4, we can see how the Arrhenius parameters relate to these isosteres: the slope of each isostere gives the energy, and the y-axis intercept gives the prefactor.

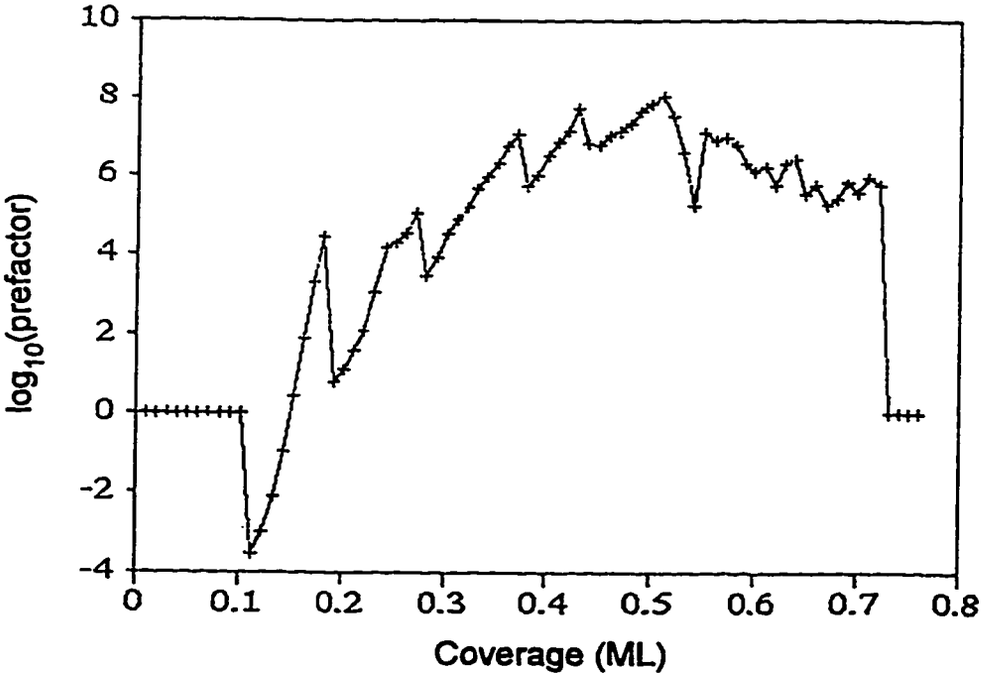

Fig. 5.4 Prefactors calculated from the isosteres in fig. 5.3, obtained with Astek [5.1].

The isosteres in figure 5.3 are for peak 1, the peak occurring at 310K-260K in figure 5.1. The slowly decreasing tail of each desorption curve moves to higher temperatures the position on the x-axis at which the area of each curve is depleted to any given coverage. This contributes to curving the isosteres, and therefore decreasing their local slope at higher temperatures. This means that the energy parameter determined

from the average slope of each isostere, and the prefactor determined from its intercept are both decreased as well. As can be seen in figure 5.4, this produces unphysically small (down to order 10^{-4} s^{-1}) effective prefactors.

We shall go no further in the details of this method as this distortion of the isosteres appears to limit severely the usefulness of this method in this case. In fact, any full peak method will be affected by similar problems. This would suggest the use of another type of method.

5.4 Threshold Method

5.4.1 Description

Although, looking at the general shape of the desorption curves, it seems that most of the gas evacuates the shroud within the time constant suggested by the width of the peaks, there is a slowly decreasing tail. This may be due to material sticking on the internal walls of the shroud and therefore coming out more slowly, in effect producing a second pumping time scale. This effect would certainly be more marked on the high temperature slope than on the beginning of the upwards sweep of any peak. In view of this, we opted for a method that concentrates on the early portion of each curve: the

threshold analysis. We are therefore counting on the fact that at the threshold portion of the peaks only a small amount of gas is in the shroud and therefore that pumping out of the shroud is not yet limited by such an effect.

The threshold method works on the basis of limiting the range in temperature over which the analysis is made to a region of negligible depletion. The ratio $(\theta_0 - \theta(t))/\theta(t)$ will be smallest for small times; this will naturally occur at the "threshold" of desorption of any given peak, so that we work in the limit of $\theta \cong \theta_0$.

The meaning of the assumptions can be better understood if we consider the coverage dependence in the desorption energy determined from the Arrhenius equation. We begin with the Arrhenius form, but include the coverage dependence in ν and E:

$$\dot{\theta} = -\nu(\theta)\cdot e^{-E(\theta)/kT} \tag{5.6}$$

and considering that:

$$T(t) = T_0 + \beta t \quad , \quad \frac{dT}{dt} = \beta \tag{5.7}$$

After differentiating with respect to T, and rearranging the terms, we get:

$$E(\theta) = -k\frac{d\left(\ln|\dot{\theta}|\right)}{d\left(T^{-1}\right)} + \frac{\dot{\theta}T}{\beta}\left(\frac{kT}{\nu(\theta)}\frac{d\nu(\theta)}{d\theta} - \frac{dE(\theta)}{d\theta}\right) \tag{5.8}$$

It becomes clear that there is more to the threshold assumption than low depletion. The first term is the experimentally determined energy:

$$E_{experimental} = -k\frac{d\left(\ln|\dot{\theta}|\right)}{d\left(T^{-1}\right)} \tag{5.9}$$

Therefore, it is assumed in the threshold method that, over the region of analysis, the desorption rate is sufficiently small so that:

$$\left|\frac{\dot{\theta}T}{\beta}\cdot\frac{kT}{\nu(\theta)}\frac{d\nu(\theta)}{d\theta}\right| << E_{experimental} \quad \text{and} \quad \left|\frac{\dot{\theta}T}{\beta}\cdot\frac{dE(\theta)}{d\theta}\right| << E_{experimental} \tag{5.10}$$

The threshold region is indeed the most likely portion of each curve to meet these requirements, but further considerations of the coverage dependence of the E and ν parameters will have to be taken into account in the interpretation of our results. In the evaluation of uncertainties, it will be necessary to consider the systematic error on the desorption energy and effective prefactor caused by the coverage variation; that is, we will have to determine if the coverage dependence of the energy and the prefactor were so large as to invalidate our fundamental assumptions.

5.4.2 Application

For this method, the analysis was performed on each desorption curve separately. Simply put, using Origin 4.1[5.2], we fitted the following equation by χ^2 minimization following the Levenberg-Marquardt algorithm:

$$P = P_0 + P_1 \times T + C \cdot \nu_{eff} \cdot e^{-E/kT} \tag{5.11}$$

First, we assumed that the depletion percentage would be sufficiently small for all peaks at one quarter of full height above background. Verification of the depletion of some representative curves demonstrated that at quarter height the depletion is approximately 5 to 7%, and at 1/8 height it is approximately 1%. Below this, very few files could be fit because the upsweep of the exponential desorption rate was barely, if at all, out of the noise in the data. Essentially, by going too low, the exponential would fit to part of the background, changing drastically the parameters determined. At heights of less than 1/16 of peak height, we therefore reached the limit of fit stability; extending or

reducing the fitting range by one point either up or down could change the resulting parameters considerably.

To minimize the effects of the overlap of peak 2 with the threshold of peak 1 as peak 2 begins to appear in the thermal desorption spectra, some specific files were fitted at fractions of peak height as small as 1/32. This is 1/32 of the height of the "visible peak", peak 1, and therefore amounts to a much larger fraction of the height of the "appearing peak", peak 2. The curve found in figure 5.6 is an example of this overlap problem; it was recorded for an initial coverage slightly greater than 1 monolayer, and we can see that peak 2 is so small that it is essentially hidden due to its proximity to peak 1.

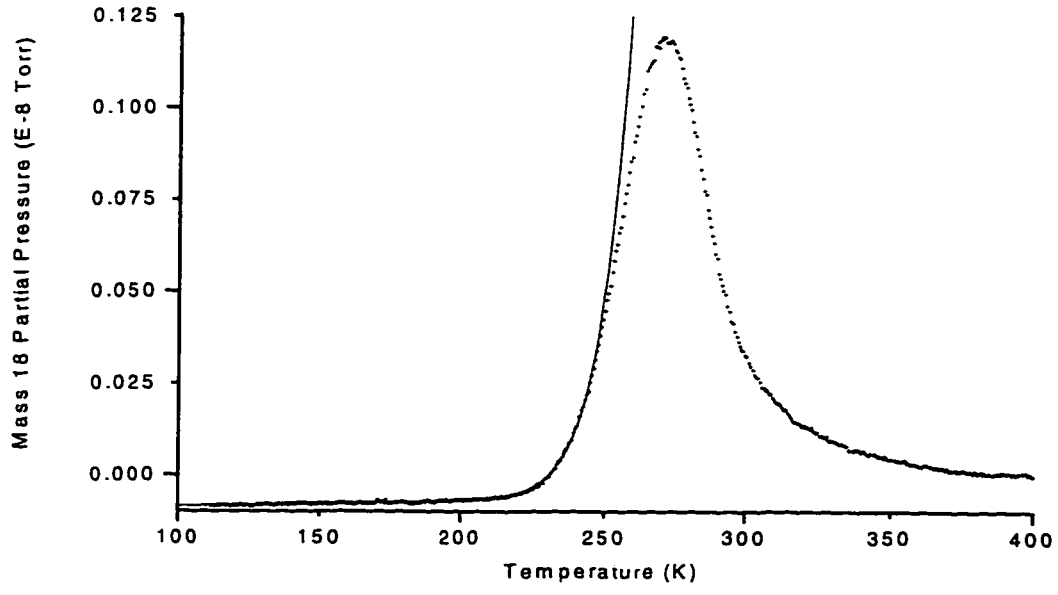

Fig. 5.5 Desorption curve for initial coverage equal to 0.53 ML. The solid line is the fit to the threshold region.

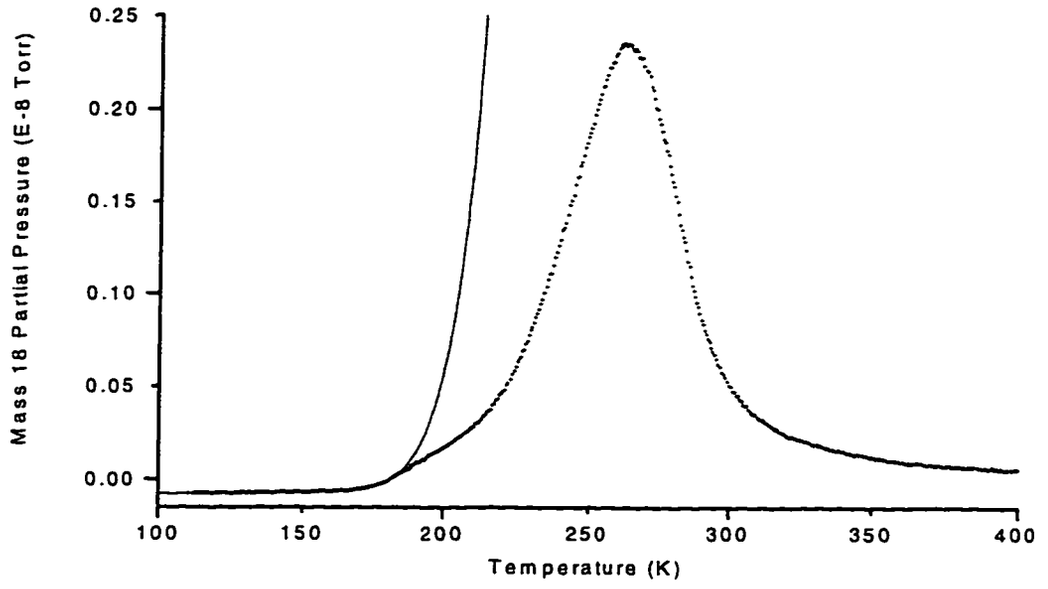

Fig. 5.6 Desorption curve for initial coverage equal to 1.17 ML. The dominant feature of the curve is peak 1 at 260K, but peak 2 can be seen emerging over the threshold of peak 1 just below 200K. The solid line is the fit to the threshold region.

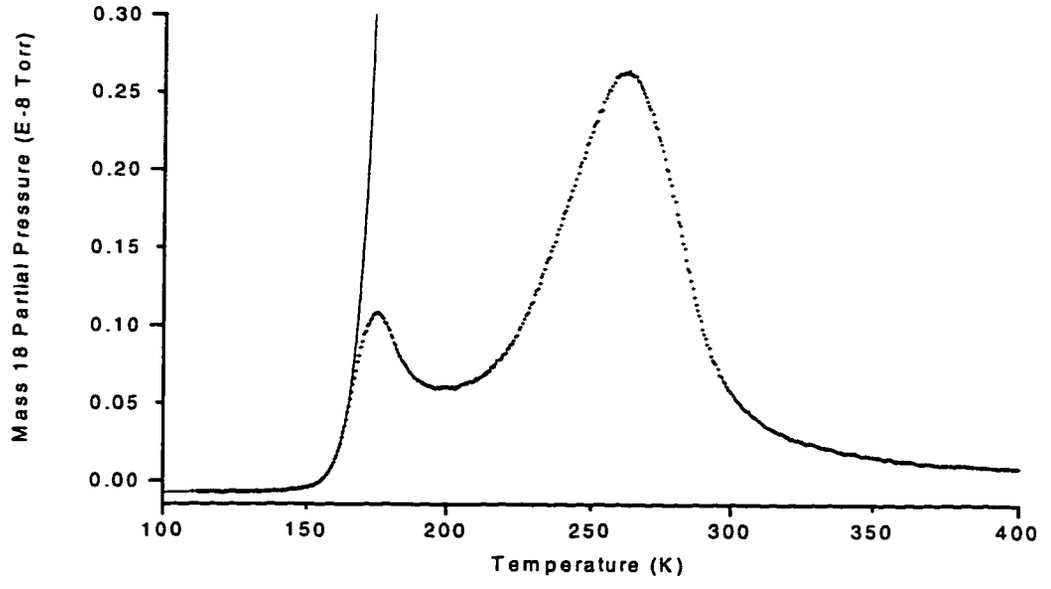

Fig. 5.7 Desorption curve for initial coverage equal to 1.62 ML. The solid line is the fit to the threshold region.

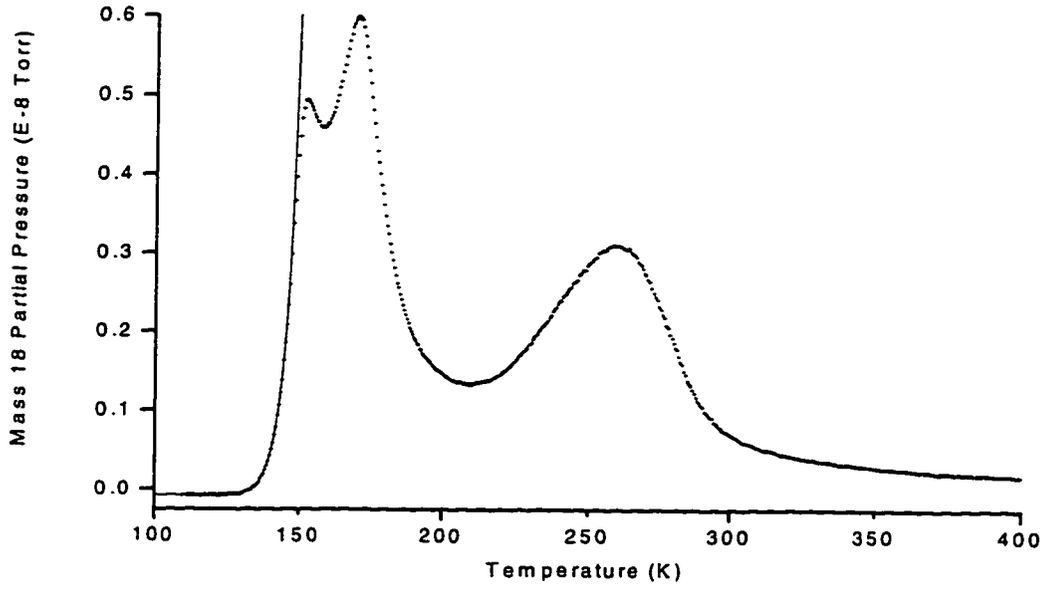

Fig. 5.8 Desorption curve for initial coverage equal to 3.40 ML. The solid line is the fit to the threshold region.

The higher coverage files have their desorption threshold lower in temperature, as can be seen in figure 5.1, and therefore the portion of the curve that can be considered to be background in the fitting procedure is much shorter. These files were fitted with the P_1 parameter in equation (5.11) set to zero, that is, with constant background. The fractions of peak height up to which the fits were performed, and the state of the P_1 parameter (fixed at 0, or free) can be found in table 5.1.

Figures 5.5, 5.7 and 5.8 show examples of fits to the three different desorption peaks in the sequence in which they appear in the thermal desorption spectra as initial coverage is increased. Each of these figures therefore represents analysis of adsorption/desorption at a different site. The adsorption sites will be discussed in greater detail in the interpretation section.

Just as all the pressures could have been divided by 15.04 Torr×s/ML to convert them into the units and scale of rate of change of coverage, it is possible to simply divide the prefactors determined by the fit to the raw data by 15.04 Torr×s/ML. This is what we did. After proper conversion of the prefactors, we graphed E and ν_{eff} versus coverage and listed the final values in table 5.1.

In figures 5.9 and 5.10 we see the result of the threshold analysis. In the coverage region associated with the first adsorption site (coverage from 0 ML to 1 ML), the Arrhenius parameters are strongly coverage dependent. Beyond coverage 1.5 ML, all the desorption energies found are approximately equal to 0.5 eV. Adsorption at the second and third type of sites are therefore comparable, at least in terms of bond energy. The second and third adsorption sites can be differentiated due to a marked change in effective prefactor.

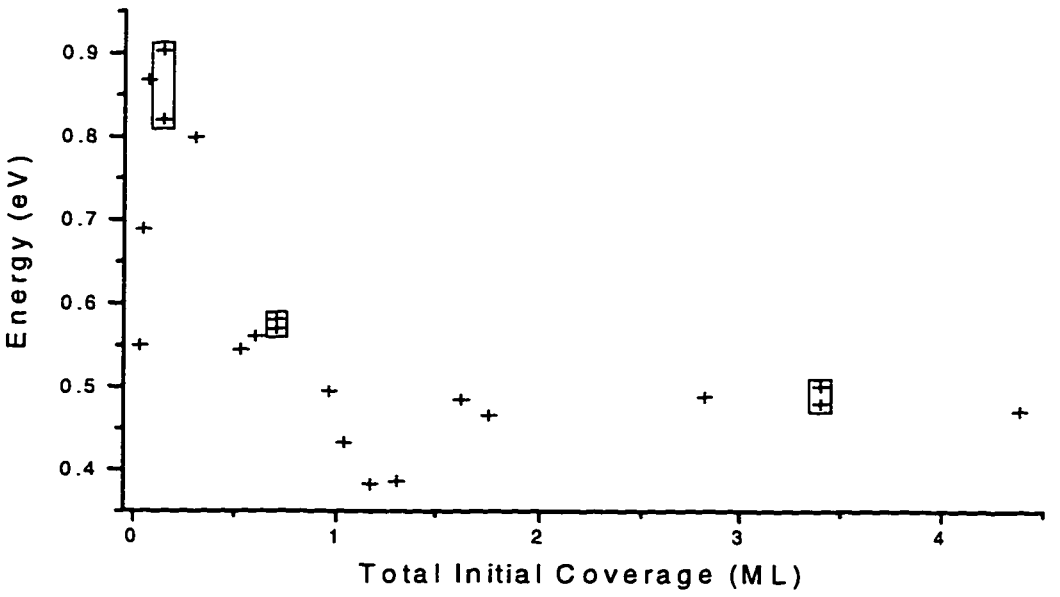

Fig. 5.9 Heat of desorption (Arrhenius parameter) as a function of coverage. The boxed points are from the files that were re-fitted at smaller fractions of peak height.

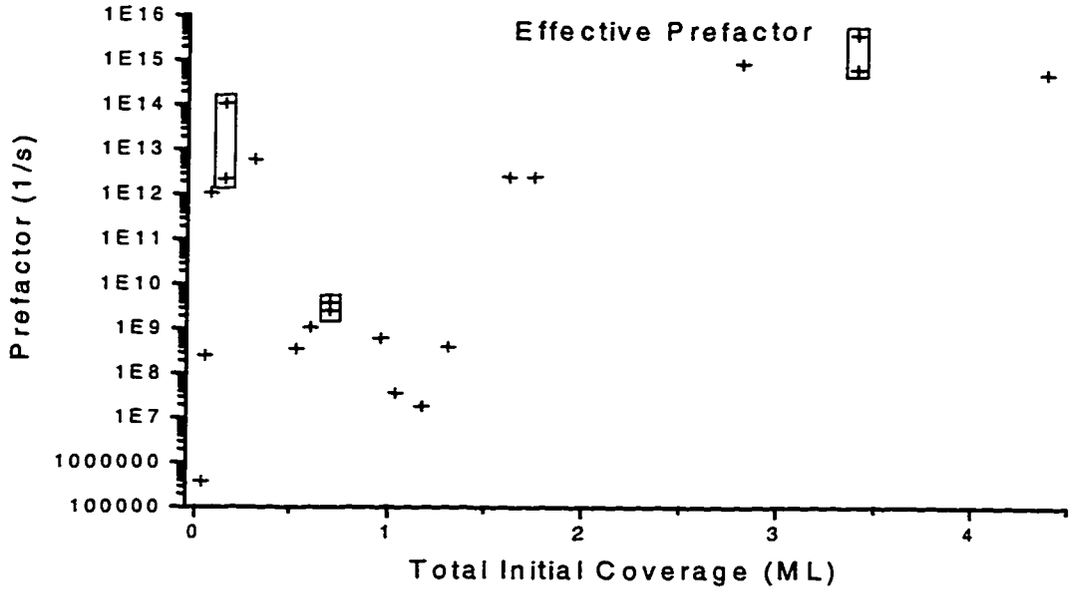

Fig. 5.10 Effective prefactor (Arrhenius parameter) as a function of coverage. The boxed points are from the files that were re-fit at smaller fractions of peak height.

5.5 Discussion on the Accuracy of the Results

As stated earlier, the fits were performed up to one quarter of the total peak height. We then evaluated the uncertainty related to the assumptions of low depletion, small desorption rate, and small change in E and ν_{eff} by fitting up to only 1/16 of peak height and, when signal to noise permitted, 1/32 of peak height. Calculations of this uncertainty based on the change in fit parameters can be found in Appendix D.

The fact that on both the energy and the effective prefactor graph a step at coverage equal to 0.3 ML separates the points in that coverage region into two small packets makes it difficult to identify a general trend for the coverage dependence in the

Arrhenius parameters. Specifically, it will be impossible to conclude on the order of the kinetics from the effective prefactor for coverages less than 1 ML.

To determine the extent of the effects of slow pumping out of the shroud mentioned in section 5.4.1, we recorded some TDS runs for which the sample was positioned 2 cm from the opening of the shroud, instead of 2 mm. Comparing the curves in figures 5.11, we can see that the width and the high temperature tail of the 300K peak (peak 1) are not changed. We therefore deduce that there is no significant effect of a possible reduction in conductance out of the shroud due to the proximity of the sample. Another experimental limitation in the same vein, would be the effect of re-adsorption onto the sample if the sample were too close to the opening in the shroud, but no evidence of this was seen.

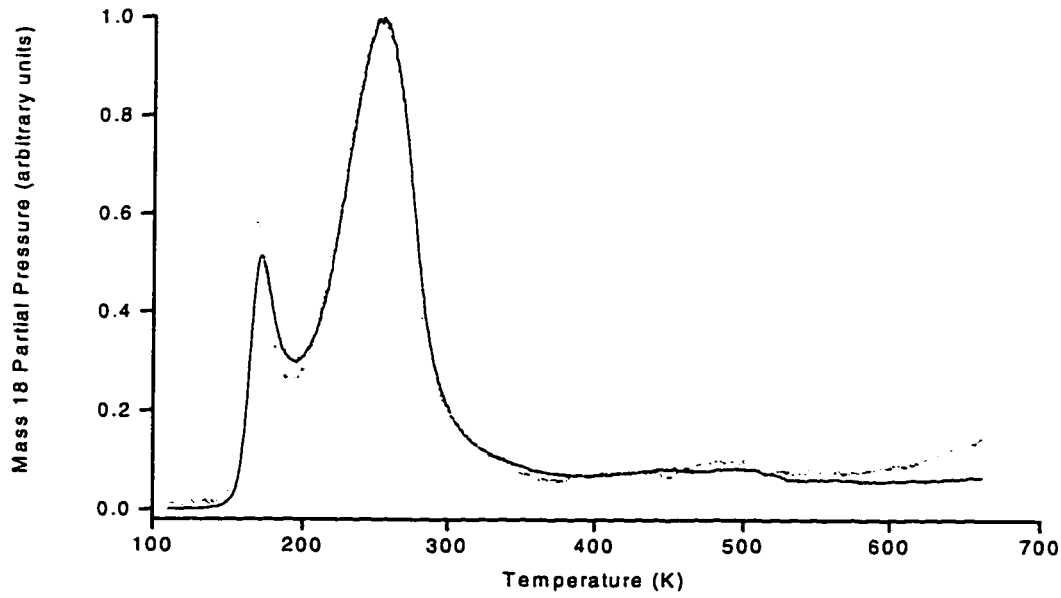

Fig. 5.11 The dashed curve was recorded with the sample 2 cm away from the shroud. The solid curve was recorded at the normal position 2 mm away from the shroud. The two curves have been normalized to a peak height equal to 1 for comparison; the dashed curve has been multiplied by a factor 5 times greater than that for the solid curve.

As stated in section 3.4.1, the shroud was designed to increase selectivity, and hence reduce the signal due to desorption from other surfaces, such as the manipulator (molybdenum) and the thermocouple glue. To test, in hindsight, the effectiveness of the shroud, we recorded some TDS runs for which the sample was dosed 2 cm away from the doser instead of 1cm (see figure 5.12); we also recorded a TDS run during which the sample was positioned so that the shroud opening lay directly over the sample glue and equally over the sample plate and the sample itself (see figure 5.13). The distortion of the TD spectrum around 210K suggests that indeed some other material close to the sample is a source of gas during the desorption runs. The shroud did then serve its purpose, but this remains a possible source of error for the curves having a threshold close to this extra feature. Even a small amount of material desorbing from another surface that fortuitously occurs at the threshold of a peak could affect our analysis greatly; the curves possibly affected are those for initial coverages less than but close to 1 ML.

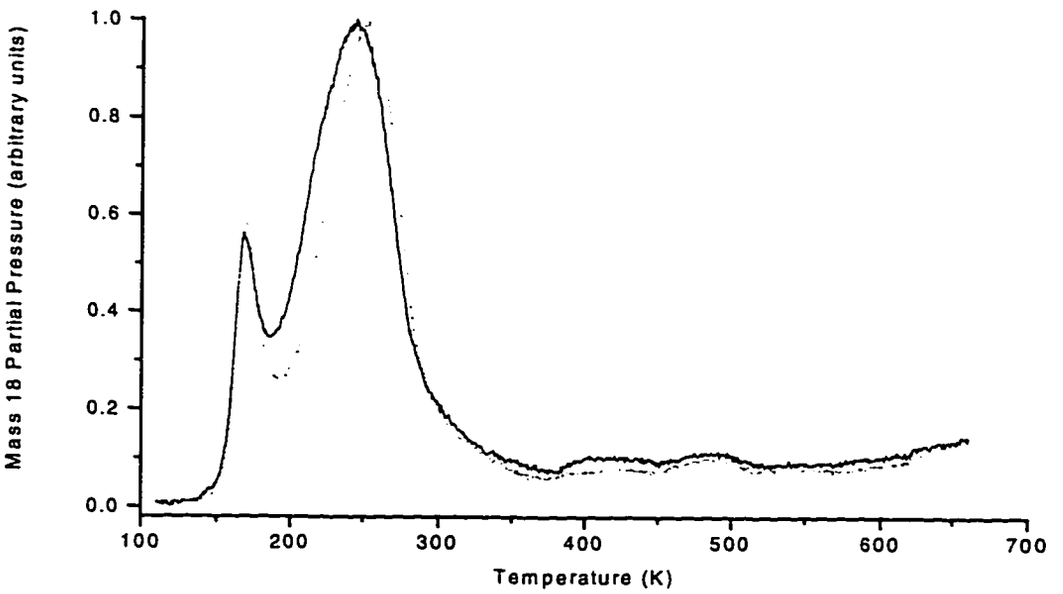

Fig. 5.12 The two curves have been normalized to a peak height equal to 1 for comparison. The solid curve was recorded after dosing the sample at 2 cm away from the doser. The dashed curve was recorded after dosing at the normal distance of 1 cm away from the doser. To accentuate the effects of this test, both curves were recorded with the sample 2 cm away from the shroud.

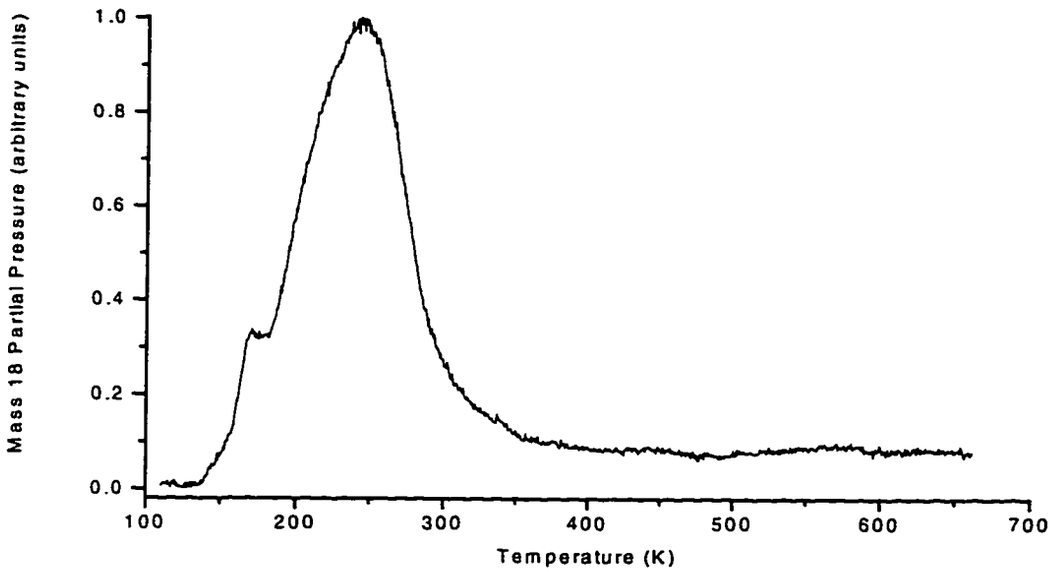

Fig. 5.13 This curve has been normalized to a peak height equal to 1. It was recorded with the opening in the shroud aimed at the thermocouple glue, the sample clip, and the sample.

Dosing and therefore adsorbing too close to the doser might have provided for a range of coverages over the surface of the sample. The fact that the downward high temperature tail of peak 1 in figure 5.12 does not change when we dose away from the doser instead of close to it is evidence that this is not so, and in fact that coverage is sufficiently uniform over the surface.

Finally, we did not work on a perfect surface, there was a certain defect density that we must consider. We roughly evaluated the defect density in chapter 4 and found it to be on the order of 10 %, but there is spectroscopic (electron spectroscopy) evidence for the lack of step effect on water adsorption [5.3]. We are also aware that there must be a small density of oxygen vacancies on the surface; the peak at 500K that can be seen on all the desorption curves in figure 5.1 is often attributed to this, but we did not concern ourselves with it in our study. The effects of the oxygen vacancies could be tested by annealing the sample in oxygen and thus reducing the surface density of oxygen vacancies.

5.6 Interpretation of Results

In figures 5.9 and 5.10, we see the coverage dependence in the Arrhenius parameters. It should be possible to determine from the graph of effective prefactor as a function of coverage the order of the kinetics involved. This would be done as:

$$\nu_{eff} = \nu \times \theta^{n}.$$

Much of our interpretation of the final results for E and ν_{eff} will require the assumption of certain models, or at least the presumption of a certain picture of what is involved at the surface. Campbell et al. propose a model based on evidence obtained with TDS, work function measurements, and X-ray Photoelectron Spectroscopy[1.4]. Because, as we did, they chose the saturation area of the 300K peak as coverage equal to 1 ML, our coverage calibrations are qualitatively similar. This will allow us to relate some of our interpretations to their model.

In the picture they propose the first site water molecules (coverage < 1ML, what we refer to as peak 1) adsorb with the oxygen atom binding to the Ti^{4+} in each surface unit cell that is only fivefold coordinated. The second site (1 ML < coverage < 2 ML, peak 2) water molecules are assumed to bond to the hydrogen of the first site water that is sticking up, and to the uppermost oxygen of the substrate in the row seen in figure 1.2; this bond is therefore similar to the hydrogen bond that links water molecules to one another in ice. Here it is important to note that the first and second site water molecules are both in contact with the TiO_2 substrate, and that properly speaking they do not form two distinct layers. This is not only related to the bonding characteristics of water, but also to the fact that, as described in chapter 1, the TiO_2 (110) surface is not perfectly flat. Further adsorbing water molecules (coverage > 2 ML, peak 3) are in contact only to other water molecules, bonding through a bond much like the hydrogen bond of ice.

In figure 5.10, we find effective prefactors of up to 10^{15} s^{-1}. Prefactors in this range are not commonly expected, but some theoretical predictions have varied from the often presupposed 10^{12} s^{-1} or 10^{13} s^{-1}. Returning to the picture of the adsorption potential well we presented in chapter 2, we can surmise the existence of an excited state, such as in transition state theories for desorption. In such models, the ratio of the entropy of the excited state over the entropy of the ground state appears in the calculations of prefactors. A transition state that is less bound, or more disordered, over the degrees of freedom than the ground state would contribute to increasing the calculated prefactor. A physical picture in which the transition state, that is, an excited state is freer along its degrees of freedom would indeed be reasonable. Even in models for point particle thermal desorption, such as the phonon mediated model we described in chapter 2, prefactors higher than 10^{13} s^{-1} can be found. These calculations involve the coupling constant for phonons to couple to the localized vibration which serves to excite the adsorbed particle. These coupling constants can vary greatly, and therefore so can the resulting prefactors. Of course the configurational differences of an excited state and the ground state also come into the calculations of the energy transfer rates in a phonon mediated desorption model.

These models do not necessarily offer the correct answer for the H_2O/TiO_2 (110) system, but they demonstrate that values such as the higher ones found in our analysis can be understood within the framework of theoretical physics. Indeed the curves recorded for the multilayer peak were not affected by any considerable difficulties in the fitting procedure. The extremely low prefactor values that were found, values less than 10^{10} s^{-1} at total coverages equal to 0.03 ML, 0.05 ML, and from 0.5 ML to 1.3 ML, on the other hand, as discussed in the previous section, were related to some of the most severe limitations in our analysis. We shall return to our interpretation of the prefactor results further in this section, when we consider each coverage region separately.

Looking at the energy graph in figure 5.9, we can see a marked increase in energy going from coverage equal to 0 ML up to 0.15 ML. We can see a similar increase at coverage slightly greater than 1 ML. Attractive interactions could have the effect of increasing the heat of adsorption from a single particle energy to the energy involving interactions with neighbors (clustering). In figure 5.1, the curves at initial coverage near 0 ML have the smallest signal to noise ratio, so that one should be wary of deducing any "physical picture" specifically from these files. The files at coverages slightly greater than 1 ML were difficult to analyze due to the overlap of the entirety of peak 2 with the threshold region of peak 1. Furthermore, at coverage 1 ML, there is a change in binding energy as the adsorption shifts from mostly site 1 to mostly site 2. Therefore, considering the assumptions described in section 5.4.1, the curves for coverages around 1 ML require an analysis at very small depletions.

There is an overall decreasing trend in the Arrhenius parameters at coverages from 0 ML to 1 ML, but the step in energy at coverage 0.3 ML makes it difficult to identify the specific shape of this trend. The two curves giving energies respectively of 0.80 eV and 0.55 eV are only 0.2 ML apart. The magnitude and the step shape in the trend could be exaggerated by the possible occurrence of desorption from another surface at the threshold of these curves. The points respectively below and above these two points, that is, the values at coverages equal to 0.15 ML and 0.7 ML, were tested by fitting at smaller fractions of peak height. As the numbers found in Appendix D demonstrate, the Arrhenius parameters at coverages equal 0.15 ML and 0.7 ML are rather stable, but the prefactor values around 0.7 ML are, as discussed earlier, extremely small. However, in the case that the step shape would be accurate, although its magnitude would be exaggerated, it could possibly indicate one of two things: 1) there are in fact two different sites in what we now call coverage region 1 ML, or, if there is only one site, 2) there is some interaction between the adsorbed particles that results in a phase transition linked

with either ordering or two different adsorption configurations for the molecule at the same type of site.

It is therefore difficult to identify the order of the kinetics from the prefactors at coverages less than one. There is an upwards trend both at coverages less than 0.3 ML and above 0.5 ML, but the error bars on these data points combined with the small number of points available if one is to look at both regions independently makes it impossible to assign a value to the exponent in $\nu_{eff} = \nu \times \theta^n$ with a reasonable level of certainty. What can clearly be said is this: There is a coverage dependence in the prefactor, and the assumption of an arbitrary value of $\nu_{eff} = 10^{12}\ s^{-1} \times \theta$ (as is often done) can only hide specific details in the physics of the system. Whether the trend is overall decreasing with coverage, or increasing in two distinct regimes remains to be determined. Campbell et al. obtained an overall decreasing trend and attributed it to an effective repulsive interaction.

The oxygen to hydrogen bond in the water molecule is 0.96 Å long, and the oxygen to oxygen distance for hydrogen bonded molecules in ice is 2.76 Å. The TiO_2 (110) surface unit cell is 2.96 Å × 6.49 Å. In the picture proposed by Campbell et al., there is only one first site water molecule per surface unit cell of the TiO_2 substrate. The water molecules could interact over the surface unit cell distances through the dipolar interaction. This could contribute to an effective repulsive interaction. Such an interaction by which there were a decrease in adsorption energy when molecules are on neighboring sites, could create a system in which every second site would be filled preferentially, giving a $\sqrt{2}\times\sqrt{2}$ overlayer. When, with increasing dose, the nearest neighboring sites would be filled, it would be with a lower binding energy. But we do not have any corroborating evidence for the existence of a superstructure (LEED measurements could be performed to study this).

We now consider the rise in both energy and prefactor at coverages from 1 ML to 1.5 ML. Picturing the second site water molecules bonded to the hydrogens sticking up from the first site water molecules and to the uppermost oxygen anions of the substrate, there is, as for the first site, only one second site molecule per surface unit cell. The increase in Arrhenius parameters from coverages 1 ML to 1.5 ML is possibly indicative of an attractive interaction. A repulsive dipolar interaction as described in the previous paragraph would not be consistent with this, and either some other effective interaction would have to be proposed or the bond configuration of the Campbell picture would have to be abandoned.

Finally, the desorption energy is the same for coverages ranging from about 1.5 ML to 4 ML (the higher coverage limit of our study). What differentiates the coverage region ranging from 1 ML to 2 ML from the region of coverages higher than 2 ML and up, is the change in prefactor at coverage equal to 2 ML. Even with the limitations discussed in the previous chapter, this increase is significant. The result that energies for the second site water, and the multilayer water are equal is consistent with the picture that both the second site water and the multilayer water adsorb through a bond much like the hydrogen bond of ice. The change in prefactor may be attributable, in this picture to the fact that one of the hydrogens in each second site water molecule is bonded to a TiO_2 substrate oxygen whereas the water molecules that bond after that bond only to other water molecules. Considering the theoretical calculations described earlier, it is not difficult to surmise that the phonon vibrational coupling constants for a molecule in direct contact with the substrate would be different from that for a molecule which is not. We therefore have a picture of the adsorbate structure quickly relaxing (within one to two layers) to a bond type much like that of ice.

CHAPTER 6
CONCLUSION

This study concentrated on all the adsorption states of water on the nearly perfect (1×1) TiO_2 (110) surface instead of concentrating strictly on the first one. In it, we therefore tried to look at the entire coverage range up to and including the multilayer, ice like adsorption of water. There is certainly much motivation for research projects aiming to study each coverage region and therefore each of the adsorption states.

The files at coverages less than one monolayer surely suggest the need for more data, and therefore a study of that coverage region alone would be in order. The details in this section of the graph of the desorption energy and effective prefactor may hint at possible details in the physics of the system.

We did not extensively search for ordering in the adsorbed layer. It is possible that the adsorbate is frozen in a state of disorder at low temperatures. An experiment studying ordering for the first site would involve adsorbing to coverages less than one monolayer and subsequently heating to temperatures just below the desorption threshold. This would anneal the overlayer, and a LEED diffraction pattern might then reveal a superstructure.

For the coverage dependent desorption peak at 310K-260K, we found energies in the range of 0.55 eV to 0.87 eV, and effective prefactors ranging from 4×10^{8} s^{-1} to 6×10^{12} s^{-1}. We also identified two possible regimes in that coverage region: the first

regime is around coverage equal to 0.2 monolayer and has an average energy of 0.83 eV and an average effective prefactor of 3×10^{12} s^{-1}, and the second regime is around coverage equal to 0.6 monolayer with an average energy equal to 0.56 eV and an average effective prefactor of 1×10^{9} s^{-1}. We believe that the Arrhenius parameters for coverages around 0.6 monolayer are exaggeratedly low.

For the desorption peak at 175K, we found an energy of 0.48 eV (+11 %, -7 %) and an effective prefactor of 3×10^{12} s^{-1} (+5 % on $\ln\nu_{eff}$). This peak does not shift in position with coverage and therefore is not due to second order kinetics, and since it saturates we do not believe that it is due to zeroth order kinetics. In the case of first order kinetics, the prefactor ν is equal to 4×10^{12} s^{-1}.

For the multilayer desorption peak at 150K, we have zeroth order kinetics with a prefactor of 7×10^{14} s^{-1} (+5 % on $\ln\nu$) and an energy of 0.48 eV (+11 %, -7 %). This value compares well to the results of other research teams for the heat of desorption found in their thermal desorption measurements for multilayer water on Ag (100) and Ag (111), Ir (110), Pt (111), and Ru (001), values for which range from 0.44 eV to 0.50 eV [6.1].

APPENDIX A
THE DATA ACQUISITION PROGRAM
(happily named TDS.BAS)

```
DEFDBL A-Z
REM $INCLUDE: 'C:\LW\INCLUDE\GRAPHICS.INC'
REM $INCLUDE: 'C:\LW\INCLUDE\FORMATIO.INC'
REM $INCLUDE: 'C:\LW\INCLUDE\LWSYSTEM.INC'
REM $INCLUDE: 'C:\LW\INCLUDE\RS232.INC'
REM $INCLUDE: 'C:\LW\INCLUDE\DATAACQ.INC'



REM ************************************************************
REM     CONFIGURE COM PORT, ATMIO16 BOARD, AND FILE
REM ************************************************************
CALL OpenComConfig (2, 9600, 2, 7, 1, 512, 512, 0, 0)
CALL SetComTime (2, .056)
t..00000% = AI.Config (1, 0, 10, 0)
a..dummy% = AI.Clear (1)
CALL SetupPrinter ("LPT1", 1, 8.0, 10.0, 1)
REM ************************************************************



REM ************************************************************
REM     INITIALISE VARIABLES
REM ************************************************************
dim range as string * 2
rem   dim mass%(10)
dim intro as string * 4
dim midle as string * 7
dim concl as string * 3
dim time1#(1400)
dim temp#(1400)
dim pressure#(1400)
dim time2#(1400)
dim tmp.dump#(2)
dim prs.dump#(2)
packet$ = chr$(&h4) + "0000" + "PV" + chr$(&h5)
dim tp as string * 10
dim p as string * 20
dim t1 as string * 20
dim t2 as string * 20
dim cyclemax as string * 10
REM ************************************************************
```

```
REM ***************************************************************
REM    INITIALISE SCREEN, AND GET INFO FOR GRAPH AND MASSES
REM ***************************************************************
CLS
PRINT "Thermal Desorption, Data Acquisition"
print
input;"Ti (xmin)";xmin
print
input;"Tf (xmax)";xmax
print
input;"dT (increment)";dx
print
input;"rate (K/s)";v
print
input;"mass spec range (10-?) (type 0 for 10, and 1 for 11)";range$
print
rem   input;"How many masses do you want followed (max # =
10)";num.masses%
cls
print "Ti ="; xmin; "K"
print "Tf ="; xmax; "K"
print "rate ="; v; "K/s"
print "increment ="; dx; "K/point"
rem   (goes on end of previous line) num.masses%
rem   i% = 1
rem   WHILE i% <= num.masses%
rem      print "mass #"; i%
rem      input;mass%(i%)
rem      i% = i% + 1
rem   WEND
REM ***************************************************************


REM ***************************************************************
REM    PREPARE REAL TIME GRAPH
REM ***************************************************************
ymin = 0
ymax = 10
CALL SetTitle ("Thermal Desorption")
CALL SetFrmColor (15)
CALL SetTtlColor (4)
CALL SetGrdColor (8)
CALL SetLblColor (1)
CALL SetBckColor (15)
CALL SetAxName (0, "Temperature (K)")
CALL SetAxScale (0, 0)
CALL SetAxAuto (0, 0)
CALL SetAxLblUnits (0, 0)
CALL SetAxRange (0, xmin, xmax, 10)
CALL SetAxName (1, "Pressure (~Torr)")
CALL SetAxScale (1, 0)
CALL SetAxAuto (1, 0)
CALL SetAxLblUnits (1, 0)
CALL SetAxRange (1, ymin, ymax, 10)
CALL GrfReset (4)
CALL SetPlotMode (0)
CALL SetCurv2D (1)
CALL SetCrvColor (2)
CALL SetPointStyle (10)
REM ***************************************************************
```

```
REM ***************************************************************
REM    READ THE TEMPERATURE AND PRESSURE, AND STORE THEM IN ARRAYS
REM ***************************************************************
i% = 0
dx = dx / 1.20
temp#(0) = xmin - dx
temp#(1) = temp#(0)
cycle% = 1
cycle.max% = 8 * fix(1000*dx/v) + 1
print "initial # of P measurements per point ="; cycle.max%
print
print "Press any key to initiate data acquisition.  I will wait for Ti."
i..dummy% = GetKey
cls
print "Have a nice day."
WHILE temp#(i%) < xmax
   i% = i% + 1
   temp#(i%) = temp#(i%-1)
   WHILE temp#(i%) < temp#(i%-1) + dx
      nout% = ComWrt (2, packet$, 8)
      CALL Delay (0)
      nin% = ComRd (2, intro$, 3)
      nin% = ComRd (2, midle$, 6)
      nin% = ComRd (2, concl$, 2)
      formatok% = Fmt (temp#(i%), "%f<%s", midle$)
   WEND
   time1#(i%) = timer
   cycle% = 1
   pressure#(i%) = 0
   WHILE cycle% <= cycle.max%
      i..dummy% = AI.VRead (1, 0, 1, rough#)
      pressure#(i%) = pressure#(i%) + rough#
      cycle% = cycle% + 1
   WEND
   pressure#(i%) = pressure#(i%)/cycle.max%
   time2#(i%) = timer
   prs.dump#(0) = pressure#(i%-1)
   prs.dump#(1) = pressure#(i%)
   tmp.dump#(0) = temp#(i%-1)
   tmp.dump#(1) = temp#(i%)
   CALL GrfCurv2D (tmp.dump#(), prs.dump#(), 2)
   now% = fix(15*v)
   past% = fix(6*v)
   diff% = now% - past% + 1
   IF i% = now% then
      a% = past%
      average.time# = 0
      WHILE a% <= now%
         average.time# = average.time# + (time2#(a%) - time1#(a%))/diff%
         a% = a% + 1
      WEND
      cycle.max% = fix(0.8*(dx/v)/(average.time#/cycle.max%)) + 1
   ENDIF
WEND
REM ***************************************************************
```

```
REM ***************************************************************
REM     SIGNAL TO USER "end of...",PRINT?, AND WRITE TO FILE
REM ***************************************************************
imax% = i%
i% = 1
formatok% = Fmt (cyclemax$, "%s<%i", cycle.max%)
CALL SetTxColor (2)
CALL GrfPrint (35, 50, "Data acquisition terminated.")
CALL GrfPrint (45, 40, cyclemax$)
CALL GrfMsg ("Press any key to continue.", 15)
i..dummy% = GetKey
CALL DeletePort (0)
CALL SetTitle ("Thermal Desorption")
CALL SetFrmColor (0)
CALL SetTtlColor (15)
CALL SetGrdColor (0)
CALL SetLblColor (15)
CALL SetBckColor (0)
CALL SetGrdFrame (1)
CALL SetAxName (0, "Temperature (K)")
CALL SetAxScale (0, 0)
CALL SetAxAuto (0, 0)
CALL SetAxLblUnits (0, 0)
CALL SetAxRange (0, xmin, xmax, 10)
CALL SetAxName (1, "Pressure (~Torr)")
CALL SetAxScale (1, 0)
CALL SetAxAuto (1, 0)
CALL SetAxLblUnits (1, 0)
CALL SetAxRange (1, ymin, ymax, 10)
CALL GrfReset (4)
CALL SetPlotMode (0)
CALL SetCurv2D (1)
CALL SetCrvColor (15)
CALL SetPointStyle (10)
CALL GrfCurv2D (temp#(), pressure#(), imax%)
CALL GrfLReset (1, 0, 0, 2)
cls
print "Writting to file."
filehandle% = OpenFile ("tpd_meas.dat", 2, 1, 1)
   i..dummy% = WriteFile (filehandle%, "t1(s)", 5)
   i..dummy% = WriteFile (filehandle%, ",", 1)
   i..dummy% = WriteFile (filehandle%, "T(K)", 4)
   i..dummy% = WriteFile (filehandle%, ",", 1)
   i..dummy% = WriteFile (filehandle%, "P(10-", 5)
   i..dummy% = WriteFile (filehandle%, range$, 1)
   i..dummy% = WriteFile (filehandle%, "Torr)", 5)
   i..dummy% = WriteFile (filehandle%, ",", 1)
   i..dummy% = WriteFile (filehandle%, "t2(s)", 5)
   i..dummy% = WriteFile (filehandle%, CHR$(10), 1)
WHILE i% <= imax%
   time1#(i%) = time1#(i%) - time1#(1)
   time2#(i%) = time2#(i%) - time1#(1)
   i% = i% + 1
WEND
i% = 1
WHILE i% <= imax%
   formatok% = Fmt (t1$, "%s<%f", time1#(i%))
   formatok% = Fmt (tp$, "%s<%f", temp#(i%))
   formatok% = Fmt (p$, "%s<%f", pressure#(i%))
   formatok% = Fmt (t2$, "%s<%f", time2#(i%))
   i..dummy% = WriteFile (filehandle%, t1$, 20)
```

```
    i..dummy% = WriteFile (filehandle%, ",", 1)
    i..dummy% = WriteFile (filehandle%, tp$, 10)
    i..dummy% = WriteFile (filehandle%, ",", 1)
    i..dummy% = WriteFile (filehandle%, p$, 20)
    i..dummy% = WriteFile (filehandle%, ",", 1)
    i..dummy% = WriteFile (filehandle%, t2$, 20)
    i..dummy% = WriteFile (filehandle%, CHR$(10), 1)
    i% = i% + 1
WEND
i..dummy% = CloseFile (filehandle%)
cls
REM ************************************************************
```

APPENDIX B
THE COMPLETE PROCEDURES LIST

1 Surface Preparation

1. With both the turbo molecular pump and the mechanical pump on and pumping on the chamber, verify that the pressure in the chamber is in the mid to low 10^{-11} Torr range as read on the B. A. ion gauge. If this is not the case, replenish the Ti sorption pump by evaporating fresh Ti.

2. Turn the sputter gun control on and degas the ion gun. Both this step and the previous one assure that a minimum of ion species other than Ar will be bombarding the sample.

3. Backfill the chamber with Ar to a pressure of about 2×10^{-5} Torr on the ion gauge.

4. Increase the emission current to the ion gun filament to about 25 mA, and using the sample manipulator, turn the sample to face the sputter gun. This combination of Ar pressure and emission current generate a sample current (to ground) of about 10 μA; this sputtering regime is maintained for 30 minutes.

5. The sample is turned to face away from the ion gun, the ion gun is then turned off, and the Ar leak into the chamber is cut off (the pressure comes back down to the 10^{-11} Torr range).

6. The sample is then annealed by increasing the sample surface temperature to T = 840K, and keeping it at that temperature for 10 minutes. T = 840K was selected because at that point the heating rate reduces quite rapidly, and that therefore any higher temperature would require an inconveniently long heating time.

7. After 10 minutes, the temperature controller is programmed to step down to T = 105K (the current to the heater element therefore falls to zero). The liquid nitrogen is, at this time, made to flow through the cooling circuit.

8. After such a preparation, a series of adsorption/desorption cycles can be performed (see section 1 of chapter 5).

Note: Alternatively, at step 6, the sample can be annealed at 710K for 60 minutes. This produces an argon free high step density surface (see sections 4.3, 4.4 and 4.5).

2 TDS Measurements

1. Verify that the temperature controller is programmed for a 1K/s ramp.

2. Adjust the cooling and wait for the sample surface temperature to reach T≅110K.

3. Open the leak valve from the H_2O container to the doser (dosing tube), and allow the pressure in the chamber to increase a few tenths of a unit on the 10^{-11} scale on the ion gauge.

4. With the sample manipulator, turn the sample to face the doser (about 1 cm away from the end of the dosing tube). The pressure in the chamber should drop back down, at least partially, to its value before the leak valve was opened; and the sample surface temperature should increase a few degrees during the dosing due to radiative heating from the dosing tube. The sample is exposed to the water vapor at sample surface temperatures of T=105 to 110K. Keep the sample facing the doser for a pre-determined interval.

5. Move the sample away from the doser, and close the leak valve. The pressure at the tip of the dosing tube, and therefore at the sample, is about 1000 fold higher than at the B. A. ion gauge. A dose of 0.5×10^{-11}Torr × 55 sec as read on the B. A. ion gauge represents about 1 Langmuir at the sample.

6. Turn the mass spectrometer on, and verify that the base pressure for mass 18 is no higher than a few$\times 10^{-11}$ Torr.

7. Wait for the sample surface temperature to cool back down to a few degrees below 110K. A 1K/s linear temperature ramp is then initiated, and the sample is turned to face the opening in the shroud of the QMS. In order not to limit conductance out of the shroud, the sample is kept at about 3 to 2 mm away from the opening.

8. Activate the data acquisition program. It is designed to wait for an initial temperature, in this case 110K, and then start recording data points at a specified interval, 0.5K for these experiments. Temperature and mass 18 partial pressure are recorded at approximately every 0.5K from 110K to 660K (roughly one 500K range is required to obtain a complete spectrum for this system, that is, to go sufficiently beyond the highest temperature peak; we initiate the T ramp just below 110K, a temperature conveniently reached with the cooling system that we have, and 660K has no methodological value other than the fact that it is selected simply to get a temperature axis with "readable" increments on the (in-process) graphical output of the acquisition program.)

9. At 660K the data acquisition program should stop taking readings and save the data recorded to the hard disk. The temperature ramp is stopped, and the sample is allowed to cool for another adsorption/desorption run. As long as the sample is heated above 600K, no water is observed to remain on the surface; no history dependence was observed in the desorption spectra or the LEED patterns.

Note: Occasionally, but not during every adsorption/desorption cycle, the LEED pattern was checked after either or both of steps 4 and 9. No deviation from the normal (1×1) LEED pattern was ever observed (but more extensive a LEED study would be required to conclude that no H_2O superstructure exists at any coverage).

APPENDIX C
CALCULATIONS
OF MEAN TERRACE WIDTHS AND STEP DENSITIES

Step densities, general equations

The number of unit cells of size a1×a2 per terrace (assuming rectangular terraces) is: $N \cong \frac{L}{a_1} \times \frac{L}{a_2}$.

Considering that each cell edge is shared between two cells, the total number of cells along the edges of a terrace is: $n \cong \frac{L}{a_1} + \frac{L}{a_2}$.

It follows then that the fraction of cells that are at a step edge is:

$$F \cong \frac{n}{N} \cong \frac{(a_1 + a_2)}{L}.$$

Terrace widths, general equations

For a correlation function following $g(x) \approx e^{-|x|/l}$,

the Fourier transform is $\tilde{g}(k) \propto \frac{1}{k^2 + \gamma^2}$,

and in this case, the FWHM from the spot profile is $\Gamma = 2\gamma = 2l^{-1}$

Based on correlation distances from an origin x_0 to -x on one side and +x on the other, we define the terrace width size as $L = 2l = 2\gamma^{-1} = 4\Gamma^{-1}$.

Now, the reciprocal lattice unit vector in the direction i has norm, $k_i = \frac{2\pi}{a_i}$,

where, as before, a_i is the unit cell length in real space.

The FWHM measured from the spot profiles in figures 4.4 and 4.5 is $\frac{\Gamma}{k_i}$,

so that $\frac{\Gamma}{k_i} = \frac{4/L}{2\pi/a_i} = \frac{2}{\pi}\cdot\frac{a_i}{L}$, and therefore $L = \frac{a_i 2/\pi}{\Gamma/k_i}$

Low Step Density Surface

From reference [4.2], the mean terrace width, $L \geq 100$ Å

And therefore: $F \leq \frac{(2.96\text{Å} + 6.49\text{Å})}{100\text{Å}} \leq 10\%$

Low Step Density Surface

From the second (wider) component of the diffraction spot profiles in figures 4.3 and 4.4, we measure: $\frac{\Gamma}{k_1} = 0.05$ and $\frac{\Gamma}{k_2} = 0.08$, and knowing that a_1 = 2.96 Å, and a_2 = 6.49 Å, we calculate that $L \cong \frac{(38\text{Å} + 52\text{Å})}{2} \cong 45\text{Å}$.

And therefore, performing the same calculation as for the high step density surface, we get that: $F \cong \frac{(2.96\text{Å} + 6.49\text{Å})}{45\text{Å}} \cong 20\%$.

APPENDIX D

CALCULATION

OF THE FINAL NUMERICAL RESULTS
AND THEIR ASSOCIATED UNCERTAINTIES

Peak 3 (multilayer desorbing at 150K)

At coverages equal to: 2.8 ML, 3.4 ML, and 4.4 ML
(0.8 ML, 1.4 Ml, and 2.4 ML for that peak separately).

We found: $E = 0.488$ eV, 0.480 eV, and 0.471eV
$\nu_{eff} = 8.51\times10^{14}$ s^{-1}, 6.20×10^{14} s^{-1}, and 4.93×10^{14} s^{-1},

which we average out to: $E = 0.480$ eV and $\nu_{eff} = 6.55\times10^{14}$ s^{-1}.

The re-fit at smaller fractions of peak height (the boxed points in figures 5.9 and 5.10) (the file at coverage 3.4 ML in table 1) gave:

$$E = 0.501 \text{ eV and } \nu_{eff} = 3.68\times10^{15} \text{ s}^{-1}.$$

We evaluate the systematic underestimation as tested by the re-fit as:

$$\frac{|0.480 - 0.501|}{0.480} = 4\ \% \qquad \text{for } E$$

$$\frac{|\ln 6.20\times10^{14} - \ln 3.68\times10^{15}|}{\ln 6.20\times10^{14}} = 5\ \% \qquad \text{for } \nu$$

We evaluate the contribution to the relative uncertainty on E due to the thermocouple reading as being about:

$$\frac{-10\text{ K}}{150\text{ K}} = 7\ \%$$

We evaluate the contribution to the relative uncertainty on ν due to the coverage calibration as:

$$\text{as much as } \frac{0.06}{0.8} = 8\ \%$$

$$8\ \% << 5\ \% \text{ on } \ln \nu$$

final value for E: $E = 0.48$ eV $\begin{pmatrix} +11\ \% \\ -7\ \% \end{pmatrix}$

final value for ν: $\nu = 6\times10^{14}\ s^{-1}$ (+5 % on ln ν)

for kinetics of order 0: $\nu = \nu_{eff}$

Peak 2 (desorption from second site, at 175K)

At coverages equal to: 1.6 ML, and 1.7 ML
(0.6 ML, and 0.7 ML for that peak separately)

We found: $E = 0.454$ eV, and, 0.566 eV
$\nu_{eff} = 2.50\times10^{12}\ s^{-1}$, and $2.50\times10^{12}\ s^{-1}$

which we average out to: $E = 0.480$ eV, and $\nu_{eff} = 2.50\times10^{12}\ s^{-1}$

We take as the systematic underestimation of the Arrhenius parameters as tested by the re-fit: the same relative value as for peak 3

We take as the relative uncertainty on E due to the thermocouple reading: the same relative value as for peak 3

We take as the contribution to the relative uncertainty on ν due to the coverage calibration as: the same relative value as for peak 3

final value for E: $E = 0.48$ eV $\begin{pmatrix} +11\,\% \\ -7\,\% \end{pmatrix}$

final value for ν_{eff}: $\nu_{eff} = 2.5\times10^{12}\ s^{-1}$ (+ 5 % on ln ν)

for kinetics of order 1, and $\theta \cong 0.65$ ML, using $\nu_{eff} = \nu\cdot\theta^{n=1}$, we have:

$\nu = 3.8\times10^{12}\ s^{-1}$ (+ 5 % on ln ν)

The uncertainty on the fit itself gives a relative uncertainty of approximately ± 2 % on ln ν. This applies to all values of ν.

Peak 1 (desorption from first site, at 260K-310K)

At coverages equal to: 0.07 ML and 0.7 ML

We found: E range of [0.55 eV, 0.87 eV]

ν_{eff} range of $[3.7\times10^{8}\ s^{-1}, 6.12\times10^{12}\ s^{-1}]$

We identify two regions, having average parameters of:

$E = 0.83$ eV, $\nu_{eff} = 3\times10^{12}\ s^{-1}$ around $\theta \cong 0.2$ ML

and $E = 0.56$ eV, $\nu_{eff} = 1.4\times10^{9}\ s^{-1}$ around $\theta \cong 0.6$ ML

So that for kinetics of order 1, we could have:

$\nu = 1.6\times10^{13}\ s^{-1}$ at $\theta \cong 0.2$ ML

and $\nu = 2.3\times10^{9}\ s^{-1}$ at $\theta \cong 0.6$ ML

and for kinetics of order 2, we could have:

$\nu = 8\times10^{13}\ s^{-1}$ at $\theta \cong 0.2$ ML

and $\nu = 3.9\times10^{9}\ s^{-1}$ at $\theta \cong 0.6$ ML

REFERENCES

1.1 The sample was prepared by: *Single Crystal Technology BV, Enschede, Netherlands.*

1.2 B.L. Maschoff, J.-M. Pan, and T.M. Madey, Surf. Sci. **259** (1991) 190-206.

1.3 M.A. Henderson, Surf. Sci. **319** (1994) 315-328.

1.4 M.B. Hugenschmidt, L Gamble and C.T. Campbell, Surf. Sci. **302** (1994) 329-340.

1.5 R.G. Breckenridge and W.R. Hosler, Phys. Rev. **91** (1953) 793-802.

2.1 A. Zangwill, *Physics at surfaces*, Cambridge University Press, New York, 1988.

2.2 H.J. Kreuzer and Z. W. Gortel, *Physisorption Kinetics*, Springer Verlag, Berlin, 1986.

2.3 D.P. Woodruff and T.A. Delchar, *Modern Techniques of Surface Science - Second Edition*, Cambridge University Press, New York, 1994.

3.1 Perkin Elmer instruction manual for Model 04-161/04-162 2 kV Sputter ion gun, fig. 1, p. 12, 1980.

3.2 Gebrauchsanweisung user's manual for Spa-LEED system, Spa-LEED, fig. 1, p. 5, 1991.

4.1 P.A. Redhead,Vacuum **12** (1962) 203-211.

4.2 B. Grossmann and P. Piercy, Phys. Rev. Lett. **74** (1995) 4487-4490.

5.1 ASTEK: Analysis and Simulation of Thermal Equilibrium and Kinetics, © Helix Science Applications, authors: H. J. Kreuzer and S. H. Payne.

5.2 Origin 4.1: Microcal™ Origin™, version 4.10 16 bit, © Microcal Software, Inc.

5.3 C.A. Muryn, P.J. Hardman, J.J. Crouch, G.N. Raiker, G. Thornton, Surf. Sci. **251/252** (1991) 747-752.

6.1 P.A. Thiel and T.E. Madey, Surf. Sci. Reports **7** (1987) 211-385.